Quasi-three-dimensional modeling of rip current systems

Kevin A. Haas,[1] I. A. Svendsen,[2] Merrick C. Haller,[3] and Qun Zhao[2]

Received 21 February 2002; revised 12 December 2002; accepted 7 April 2003; published 8 July 2003.

[1] The focus of the paper is the analysis of the flow in rip current systems generated by channels in longshore bars on a beach. The horizontal variations of rip current systems are described through the use of the quasi-three-dimensional nearshore circulation model SHORECIRC. Model predictions are compared to laboratory measurements of waves and current velocities throughout the entire rip current system and show reasonable agreement. The rips in the two channels are found to behave differently because of the depth variation across the basin. It is found that higher bottom stress leads to more stable flow where the rip current meanders less and fewer eddies are generated. The wave current interaction creates forcing which reduces the distance rip currents flow offshore and can lead to a slow pulsation of the rip current. This pulsation is in addition to the instabilities of a jet which can also be present in rip currents. The three dimensionality of the rip current system is found to have a significant effect on the overall circulation patterns. *INDEX TERMS:* 4255 Oceanography: General: Numerical modeling; 4512 Oceanography: Physical: Currents; 4546 Oceanography: Physical: Nearshore processes; *KEYWORDS:* rip currents, nearshore circulation, numerical modeling, waves

Citation: Haas, K. A., I. A. Svendsen, M. C. Haller, and Q. Zhao, Quasi-three-dimensional modeling of rip current systems, *J. Geophys. Res.*, *108*(C7), 3217, doi:10.1029/2002JC001355, 2003.

1. Introduction

[2] The nearshore is a dynamic area which serves as an enjoyable leisure destination and yet contains many hazards for humans. According to the American Lifesaving Association, 80% of all rescues by lifeguards at surf beaches are the result of swimmers being caught in rip currents. Rips also play an important role in the morphodynamical changes on a littoral beach such as the cross-shore migration of longshore bars. Extensive field observations show that rip current systems form an integral part of the nearshore circulation patterns that are responsible for such morphodynamical changes [see, e.g., *Short*, 1979; *Wright and Short*, 1984; *Lippmann and Holman*, 1990].

[3] The concept of rip currents being a separate phenomena from undertow was introduced by *Shepard* [1936], and the first comprehensive observations of rips were made by *Shepard et al.* [1941] along the coast in southern California. Since then, rip currents have frequently been observed in field investigations [e.g., *Shepard and Inman*, 1950; *McKenzie*, 1958; *Sonu*, 1972; *Dette et al.*, 1995; *Smith and Largier*, 1995; *Aagaard et al.*, 1997; *Brander*, 1999].

[4] While the qualitative aspects of rip current circulations have been well described, it is equally well established that comprehensive quantitative field measurements are difficult. Therefore laboratory experiments have been used to obtain extensive measurements of rip current systems. Rip current experiments have been performed by *Bowen and Inman* [1969], *Hamm* [1992], and *Drønen et al.* [2002]. The most comprehensive laboratory measurements of rip currents to date were obtained by *Haller et al.* [2002]. These measurements were made in a directional wave basin with a longshore bar and two rip channels using several incident wave conditions. The flow velocity, wave height, and mean water level were measured over a large area, creating a detailed picture of the circulation pattern of the rip current system. The circulation was shown to consist of a primary feeder/rip system and a counter-rotating secondary circulation located closer to shore. In addition, these rip currents were found to exhibit low-frequency oscillations, and *Haller and Dalrymple* [2001] demonstrated that some of the measured oscillatory modes agreed with predictions from a rip current instability model.

[5] There have been several attempts to analyze rip currents theoretically, examining flow features such as the narrowing of rip currents due to the conservation of potential vorticity [*Arthur*, 1962], the need for longshore variability in forcing [*Bowen*, 1969; *Dalrymple*, 1978], and the importance of wave current interaction [*Dalrymple and Lozano*, 1978]. Rip current systems have also been numerically modeled previously [e.g., *Noda*, 1974; *Tanaka and Wada*, 1984], but those models did not include the effect of vertically varying currents. *Chen et al.* [1999] modeled rip current experiments with a Boussinesq model but only simulated a small portion of the basin for a short time span, and the Boussinesq

[1]Georgia Tech Regional Engineering Program, Savannah, Georgia, USA.
[2]Center for Applied Coastal Research, University of Delaware, Newark, Delaware, USA.
[3]Civil, Construction and Environmental Engineering, Oregon State University, Corvallis, Oregon, USA.

0148-0227/03/2002JC001355$09.00

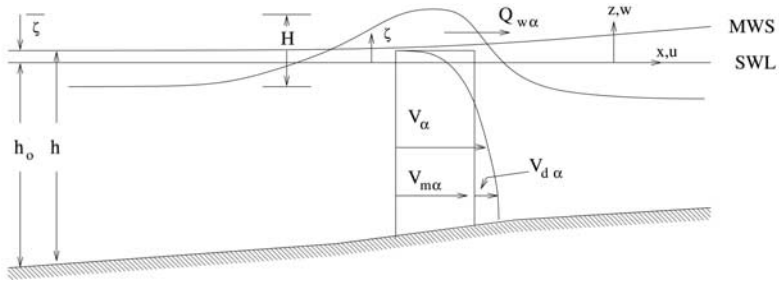

Figure 1. Definition sketch.

approach does not include the lateral mixing caused by the three-dimensionality of the current motion.

[6] The present study simulates the rip current system from the *Haller et al.* [2002] experiments using the quasi-three dimensional (quasi-3D) SHORECIRC circulation model (SC). The time-averaged horizontal flow properties from the model are verified with direct comparisons to the measurements. The simulations of the vertical variation of the rip currents were previously verified by *Haas and Svendsen* [2000] and *Haas et al.* [2000].

[7] The paper is organized as follows. The outline of the SC model version 2.0 is presented in section 2. In section 3 the time-averaged characteristics of the rip currents measured in the laboratory experiment are discussed, with comparisons between computed and measured currents and surface elevations. Section 4 discusses the differences between the rips in the two channels. Section 5 analyzes the sensitivity of the flow to changes in bottom shear stress, and section 6 gives a description of the importance of the wave current interaction. In section 7 the effect of the 3D dispersive mixing caused by the depth varying currents is analyzed. The conclusions are summarized in section 8.

2. Model Formulation

[8] The quasi-3D model system consists of a short-wave transformation component ("wave driver") and a short wave-averaged component, working simultaneously to simulate the short and long wave motions, currents and their interactions, in the nearshore regions. The quasi-3D class of models include the effect of the vertical variation of the currents within a depth-integrated model. This includes the wave-current interactions and the current-current interactions. The vertical variation of the currents are determined to second order; therefore the model includes the full effects of the 3D flow field.

2.1. Depth-Integrated Wave-Averaged Equations

[9] The derivation of the wave-averaged depth-integrated mass and horizontal momentum equations for depth varying currents uses the procedure outlined by *Putrevu and Svendsen* [1991]. This procedure is essentially identical with the methods of *Phillips* [1977] and *Mei* [1983] except that it includes the vertical variation of the currents.

[10] In the present version of the model the total velocity u_α is split into four components

$$u_\alpha = u'_\alpha + u_{w\alpha} + V_\alpha \tag{1}$$

$$V_\alpha = V_{m\alpha} + V_{d\alpha}, \tag{2}$$

where u'_α represents the velocity variations with subgrid length scale, $V_{m\alpha}$ is the depth mean current velocity, $V_{d\alpha}$ is the depth varying part of the current velocity, and $u_{w\alpha}$ is the short-wave component. The distribution of the short-wave velocity is defined such that $\overline{u_{w\alpha}} = 0$ below trough level [*Phillips*, 1977], where the overbar represents a time average over a wave period.

[11] The depth mean current $V_{m\alpha}$ is defined as

$$V_{m\alpha} \equiv \frac{\overline{Q}_\alpha - Q_{w\alpha}}{h}, \tag{3}$$

the total volume flux is defined as

$$\overline{Q}_\alpha \equiv \overline{\int_{-h_o}^{\zeta} u_\alpha dz}, \tag{4}$$

and the wave induced volume flux is defined as

$$Q_{w\alpha} \equiv \overline{\int_{\zeta_t}^{\zeta} u_{w\alpha} dz}, \tag{5}$$

where z is the vertical coordinate defined as positive up from the still water level (SWL), h_o is the still water depth, ζ is the instantaneous surface, and ζ_t indicates the trough level, as shown in Figure 1. It is implied by equation (3) that

$$\overline{\int_{-h_o}^{\zeta} V_{d\alpha}\, dz} = 0. \tag{6}$$

[12] On the basis of these definitions, the wave-averaged, depth-integrated equations are as follows:

$$\frac{\partial \bar{\zeta}}{\partial t} + \frac{\partial \overline{Q}_\alpha}{\partial x_\alpha} = 0 \tag{7}$$

and

$$\frac{\partial \overline{Q}_\alpha}{\partial t} + \frac{\partial}{\partial x_\alpha}\left(\frac{\overline{Q}_\alpha \overline{Q}_\beta}{h}\right) + \frac{\partial}{\partial x_\beta}\overline{\int_{-h_o}^{\zeta} V_{d\alpha} V_{d\beta} dz} + \frac{\partial}{\partial x_\beta}\overline{\int_{\zeta_t}^{\zeta} u_{w\alpha} V_{d\beta} + u_{w\beta} V_{d\alpha} dz} = -gh\frac{\partial \bar{\zeta}}{\partial x_\alpha} - \frac{1}{\rho}\frac{\partial}{\partial x_\beta}\left[S'_{\alpha\beta} - \overline{\int_{-h_o}^{\zeta} T_{\alpha\beta} dz}\right] + \frac{\tau^S_\alpha}{\rho} - \frac{\tau^B_\alpha}{\rho}, \tag{8}$$

where α and β are indices for the horizontal directions, ρ is the water density, $T_{\alpha\beta}$ is the turbulent stress, and τ_α^S and τ_α^B are the surface and bottom shear stresses in the α direction. The modified radiation stress $S'_{\alpha\beta}$ is defined as

$$S'_{\alpha\beta} \equiv \overline{\int_{-h_o}^{\zeta} p\delta_{\alpha\beta} + \rho u_{w\alpha} u_{w\beta}\, dz} - \delta_{\alpha\beta}\frac{1}{2}\rho g h^2 - \frac{Q_{w\alpha}Q_{w\beta}}{h}. \quad (9)$$

For depth uniform currents, this definition of the radiation stress is identical with the definition used by *Phillips* [1977].

[13] The momentum equations given by equation (8) are all in terms of depth-averaged properties except for the integral terms, which represent the current-current and wave-current interaction. We solve the local horizontal momentum equations analytically over the vertical to get expressions for the depth-varying current $V_{d\alpha}$ in terms of the depth-averaged properties to use in the integrals. The derivation of the vertical variation of the currents closely follows the method of *Putrevu and Svendsen* [1999].

[14] The governing equations are solved numerically using finite differences. We use a third-order Adams-Bashforth predictor method and a third-order Adams-Bashforth-Moulton corrector method for the time derivatives [*Hoffman*, 1992]. Fourth-order central derivatives are used in space. Detailed analysis on the stability and accuracy of this method as used in SC is given by *Sancho and Svendsen* [1997]. The small-scale disturbances resulting from using finite differences to solve nonlinear equations are removed using the sixteenth-order filter given by *Shapiro* [1970].

2.2. Closure Models

[15] This subsection discusses the closure models used for completing the governing equations in SC. A more thorough discussion on most of these models is given by *Sancho and Svendsen* [1997].

2.3. Short-Wave Model

[16] The short-wave forcing represents the time-averaged contribution from the waves to the momentum balance. The derivations of the equations make no assumptions as to how the waves are modeled. The wave model REF/DIF 1 [*Kirby and Dalrymple*, 1994] is used here as the wave driver. It accounts for the effects of bottom induced refraction-diffraction, current induced refraction, wave breaking dissipation, and bottom friction dissipation by solving the parabolic equation initially developed by *Kirby and Dalrymple* [1983]. The offshore wave height, direction, and period are specified along the offshore boundary.

[17] Since the wave and current field are formally decoupled, it is necessary to periodically update the circulation field used as input to the wave model. Several different update intervals (30, 100, 250, and 500 time steps) were tested, and an interval of 250 time steps corresponding to around 7.8 s was selected. This interval is short enough to prevent large changes in the wave field between updates, and it produces similar basic results as intervals of 30 and 100 time steps.

[18] Radiation stresses represent the excess momentum flux due to the short wave motion and it is the radiation stress gradients that serve as the major source of current forcing. The REF/DIF model uses linear (sine) wave theory to calculate the wave characteristics throughout the domain, and these characteristics are in turn used to calculate the momentum and volume fluxes in SC. In the surf zone, REF/DIF utilizes a depth-limited breaking criterion (typically a wave height to water depth ratio $H/h = 0.78$) to predict the breaking pattern. However, since linear theory generally underestimates the wave heights at the break point, here we set $H/h = 0.55$ in order to best match the breaking pattern observed in the experiments. As described in later sections, the comparison of the predicted wave height and the measured data using this value is reasonable and can be seen in Figures 6 and 17 (in sections 3 and 6, respectively) for both longshore and cross-shore sections. We also include the contribution of the roller to the momentum and volume flux by using the formulations from *Svendsen* [1984a, 1984b]. Through comparisons between measurements and model simulations (shown later in section 3), we find that this gives the closest representation of the wave height gradients and of the cross-shore set-up variation (which is a close measure of the radiation stress variation, which represents the forcing).

2.4. Bottom Shear Stress

[19] In nearshore flows, both the waves and currents create bottom shear stresses, so the combined effect needs to be modeled. We use the formulation for wave-averaged bottom shear stress for combined currents and waves given by *Svendsen and Putrevu* [1990]. The result for the wave-average bottom shear stress $\overline{\tau_\alpha^B}$ can be written as

$$\overline{\tau_\alpha^B} = \frac{1}{2}\rho f_{cw} u_0 (\beta_1 V_{b\alpha} + \beta_2 u_{0\alpha}), \quad (10)$$

where f_{cw} is the friction factor for waves and currents and β_1 and β_2 are weighting factors for the (vectorial) contributions from the wave bottom velocity $u_{o\alpha}$ and the bottom current velocity $V_{b\alpha}$, respectively.

[20] For sinusoidal phase motion of the bottom velocity $u_{o\alpha}$, the weight factors for the current and wave motion β_1 and β_2 are given by

$$\beta_1 = \overline{\left[\left(\frac{V_b}{u_0}\right)^2 + 2\frac{V_b}{u_0}\cos\theta\cos\mu + \cos^2\theta\right]^{1/2}} \quad (11)$$

$$\beta_2 = \overline{\cos\theta\left[\left(\frac{V_b}{u_0}\right)^2 + 2\frac{V_b}{u_0}\cos\theta\cos\mu + \cos^2\theta\right]^{1/2}}, \quad (12)$$

where μ is the angle between the waves and the currents at the bottom and θ is the wave phase $\theta = \omega t - \int \vec{k}\cdot d\vec{x}$ with ω being the wave frequency.

2.5. Turbulence

[21] The wave-averaged subgrid stress is modeled using an eddy viscosity formulation given by

$$T_{\alpha\beta} = \rho(\nu_t + \nu_s)\left(\frac{\partial V_\beta}{\partial x_\alpha} + \frac{\partial V_\alpha}{\partial x_\beta}\right). \quad (13)$$

The eddy viscosity has two components: ν_t represents the turbulence created by the bottom friction and the breaking waves, and ν_s represents the turbulence created by the horizontal shear in the flow.

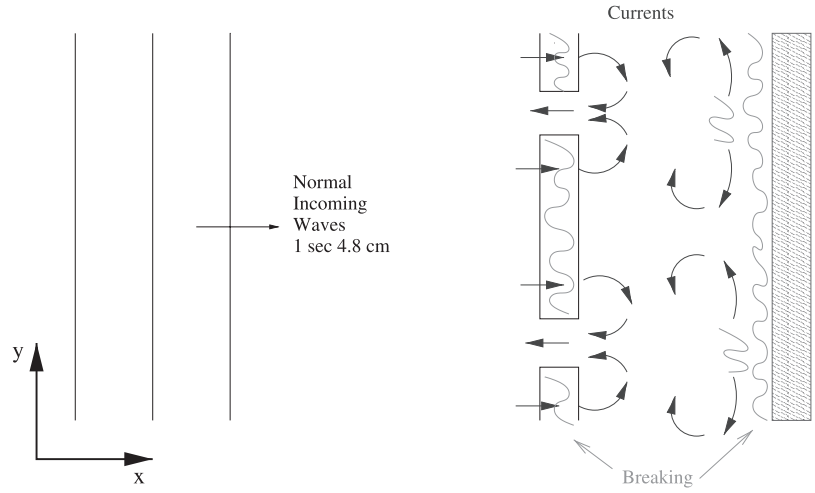

Figure 2. Schematic diagram of wave-averaged flow on a barred beach with rip channels.

[22] A detailed analysis on ν_t is given by *Sancho and Svendsen* [1997] and is only summarized here. The bottom induced turbulence is based on work by *You* [1994] and *Coffey and Nielsen* [1984]. For the turbulence from breaking Waves, a modified *Battjes* [1975] model is utilized. The combined formulation is written as

$$\nu_t = C_1 \kappa \sqrt{\frac{f_{cw}}{2}} u_0 h + Mh\left(\frac{D}{\rho}\right)^{1/3} + \nu_{t,0}, \tag{14}$$

where κ is the von Karman constant ($\kappa \simeq 4$), f_{cw} is the friction factor, D is the energy dissipation in the breaking waves, $\nu_{t,0}$ is a small empirical background eddy viscosity, and C_1 and M are constant coefficients. It is apparent that the first term on the right-hand side of equation (14) represents the bottom induced turbulence and the second term represents the wave induced turbulence. On the basis of the experiments of *Nadaoka and Kondoh* [1982] and the estimates of *Svendsen* [1987], we typically use values for the constant coefficients of $M = 0.1$ and $C_1 = 0.2$.

[23] The eddy viscosity based on the horizontal shear in the flow (ν_s) models the dissipation from the eddies which are too small to be resolved by the numerical grid. We use the Smagorinsky eddy viscosity model, first introduced by *Smagorinsky* [1963], which is written as

$$\nu_s = (C_s \Delta)^2 \sqrt{2 e_{\alpha\beta} e_{\alpha\beta}}, \tag{15}$$

where $e_{\alpha\beta}$ is given by

$$e_{\alpha\beta} = \frac{1}{2}\left(\frac{\partial V_\alpha}{\partial x_\beta} + \frac{\partial V_\beta}{\partial x_\alpha}\right). \tag{16}$$

C_s is the Smagorinsky coefficient, and Δ is the characteristic length scale of the smallest resolvable eddy.

3. Time-Averaged Properties

[24] We are using the model to simulate the circulation patterns induced by normally incident waves on a beach with a longshore bar and rip channels. Figure 2 shows a schematic diagram outlining the general flow patterns for rip current systems on such a beach. As the waves propagate toward the shore they start breaking over the bars, as indicated in the figure, creating a setup in the mean water level. The waves are not breaking as much in the channels; therefore the mean water level is lower in the channels, which creates a longshore pressure gradient from the bars directed toward the channels. This pressure gradient is driving the currents toward the channels, creating the feeder currents for the rips.

[25] The propagation of the uniform wave train over the longshore bars and channels and the variable degrees of dissipation in these areas induces a longshore variability in wave height close to the shoreline. The high waves shoreward of the channels break earlier than the waves behind the bar. This creates a larger setup near the shoreline, or a bump in the mean water level, resulting in a longshore pressure gradient which drives flow away from the channels, creating secondary or recirculation cells close to the shoreline. The circulation is highly dependent on the breaking pattern; if the waves do not break on the bar, then the mechanism outlined above is eliminated. Conversely, if the waves also break strongly in the channel, the longshore surface gradients can be reduced as well as the rips.

[26] The present study provides direct comparisons with laboratory data from a subset of the measurements corresponding to Test B from *Haller et al.* [2002]. These experiments are for normal incident waves with an offshore wave height of 4.1 cm and period of 1 s. The topography under consideration is taken from a detailed survey in the wave basin and is shown in Figure 3. The bottom was intended to be plane and the two rip channels were intended to be symmetric and equal to each other, but they clearly have some differences. The bars also exhibit longshore nonuniformities which have an impact on the circulation.

[27] The model grid spacing is $\Delta x = 20$ cm and $\Delta y = 20$ cm, and the time step is $\Delta t = 0.031490$ s corresponding to a Courant number of 0.5 at the largest depth. Several different grid sizes were tested (10, 20, and 25 cm) and 20 cm was found to be the largest size which did not change the basic results. The model is run for 52,001 time steps or 1637.48 s, virtually identical to the length of the experimental runs. In

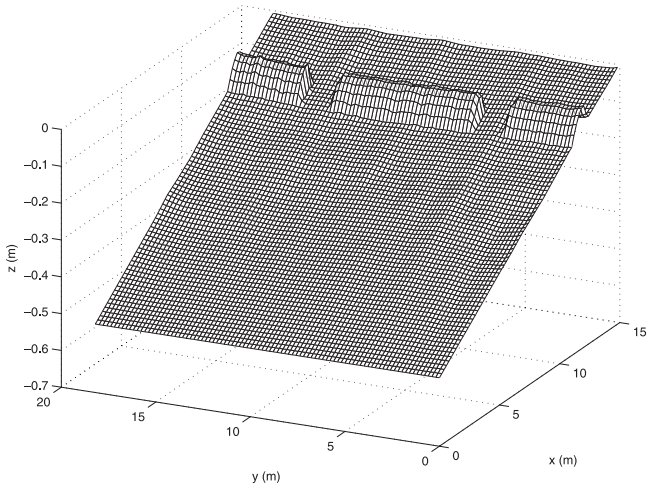

Figure 3. Topography interpolated from a survey of the wave basin.

addition, the time averages of the model and experimental data are done over the second half of the run to avoid start-up effects. The friction factor and eddy viscosity coefficients are based on standard values which can be found in the literature and are as follows unless otherwise noted: $f_{cw} = 0.01$, $C_1\kappa = 0.08$, $M = 0.1$, and $C_s = 0.15$. The boundary conditions on all four sides are standard wall boundaries where the flux into the wall is zero, and the gradient of the mean water normal to the wall is zero.

[28] The unstable nature of rip currents in the model simulations is seen in Figure 4, which shows eight snapshots of computed velocity and vorticity. The model simulation shows that the rip continually meanders side-to-side and sheds vortices that propagate offshore. The general circulation patterns will be interpreted using a long time average of these highly variable current fields. We will, however, return to the time variations later in the paper.

[29] The velocities from the experiments, generally measured 3 cm from the bottom, and the depth-integrated current $V_{m\alpha}$ from the model are displayed in Figure 5. Owing to the limited number of velocity gauges available, this picture is based on many repeated runs of the experiment with identical wave conditions but different measuring locations. The flow pattern from the model looks similar to the measured flow field. To facilitate the comparison between the model and the data, Figure 5c shows the currents from the model only at the locations where the measurements were made. The figure shows that the recirculation cells close to the shoreline have similar dimensions and the flow along the offshore edge of the central bar is parallel to the shore. Also, in both the measurements and the model results the upper rip is biased toward the inside of the basin. However, in the channel the modeled rip has a stronger longshore component than the measurements indicate.

[30] Owing to the limited number of gauges available for the measurements, it is not possible to generate a picture of the horizontal structure of the highly unsteady flow patterns using the measured data. Therefore direct comparisons between the experiments and model are only possible for the time-averaged quantities. Figure 6 shows comparisons of the wave height between the laboratory data and the model along five longshore sections. The sections are (Figure 6a) close to the shoreline, (Figure 6b) in the trough behind the bar, (Figure 6c) over the bar, (Figure 6d) on the seaward edge of the bar, and (Figure 6e) 1 m offshore of the bar. The bar is located between $x = 11$ and $x = 12.4$ m. All four sections demonstrate reasonable agreement between the model and measurements. We notice in particular that the increase of the wave height across the channel at $y \cong 13.6$ m is modeled well in Figure 6b.

[31] In order to quantify accuracy of the modeled wave height, we utilize the index of agreement between model/data as proposed by *Wilmott* [1981]. This is written as follows

$$d = 1 - \frac{\sum_{j=1}^{n} [y(j) - x(j)]^2}{\sum_{j=1}^{n} [|y(j) - \bar{x}| + |x(j) - \bar{x}|]^2}, \qquad (17)$$

where $x(j)$ are the measured data, $y(j)$ are the computed data, and $\bar{x}$ is the mean of $x(j)$. A value of $d = 1$ indicates perfect agreement, and a value of $d = 0$ indicates total disagreement. When computing d, all the measured points are used, not just the ones shown in the figures. The value of d_H for the wave height turns out to be 0.96 which is virtually identical to the value achieved by the Boussinesq model of *Chen et al.* [1999], which indicates that the wave model does a reasonable job of simulating the experimental conditions.

[32] Comparisons between the experimental data and the model results of the mean water level are shown in Figure 7. This figure shows longshore sections from near the shoreline (Figure 7a) to about 1 m seaward of the bar (Figure 7d). The agreement for all four sections is fair. In the trough region (Figure 7b) the depression in $\bar{\zeta}$ near the channel ($y \sim 13.6$ m) is modeled well. Near the shoreline in Figure 7a the computed setup is slightly overpredicted, perhaps from the use of the no flux shoreline boundary condition in the model simulation. The mean water level has a $d_\zeta = 0.96$, which again suggests that the pressure gradients are modeled fairly well.

[33] The cross-shore velocity from the experimental measurements and the computed cross-shore currents are compared in Figure 8. In general, the agreement is fairly good for the four longshore sections. Close to the shoreline in Figure 8a the longshore variation is modeled well. In the trough, however, the cross-shore currents are less accurately represented. Along the offshore edge of the bar in Figure 8c the model appears to catch the important details of the current variation. The section farthest offshore (Figure 8d) is also modeled fairly well. The computed current velocities show the rip velocity being stronger than the measurements; however, this is likely due to the measurements being lower in the water column, and therefore probably do not correspond with the actual depth-averaged velocity. As shown by *Haas and Svendsen* [2002], the rip current tends to become a surface current as it flows offshore. Hence at this position offshore of the bar the computational results may be closer to reality than the measurements indicate.

[34] More detailed comparisons of the cross-shore currents within the rip channel are shown in Figure 9. It appears that the modeled width of the rip is a little narrower than the

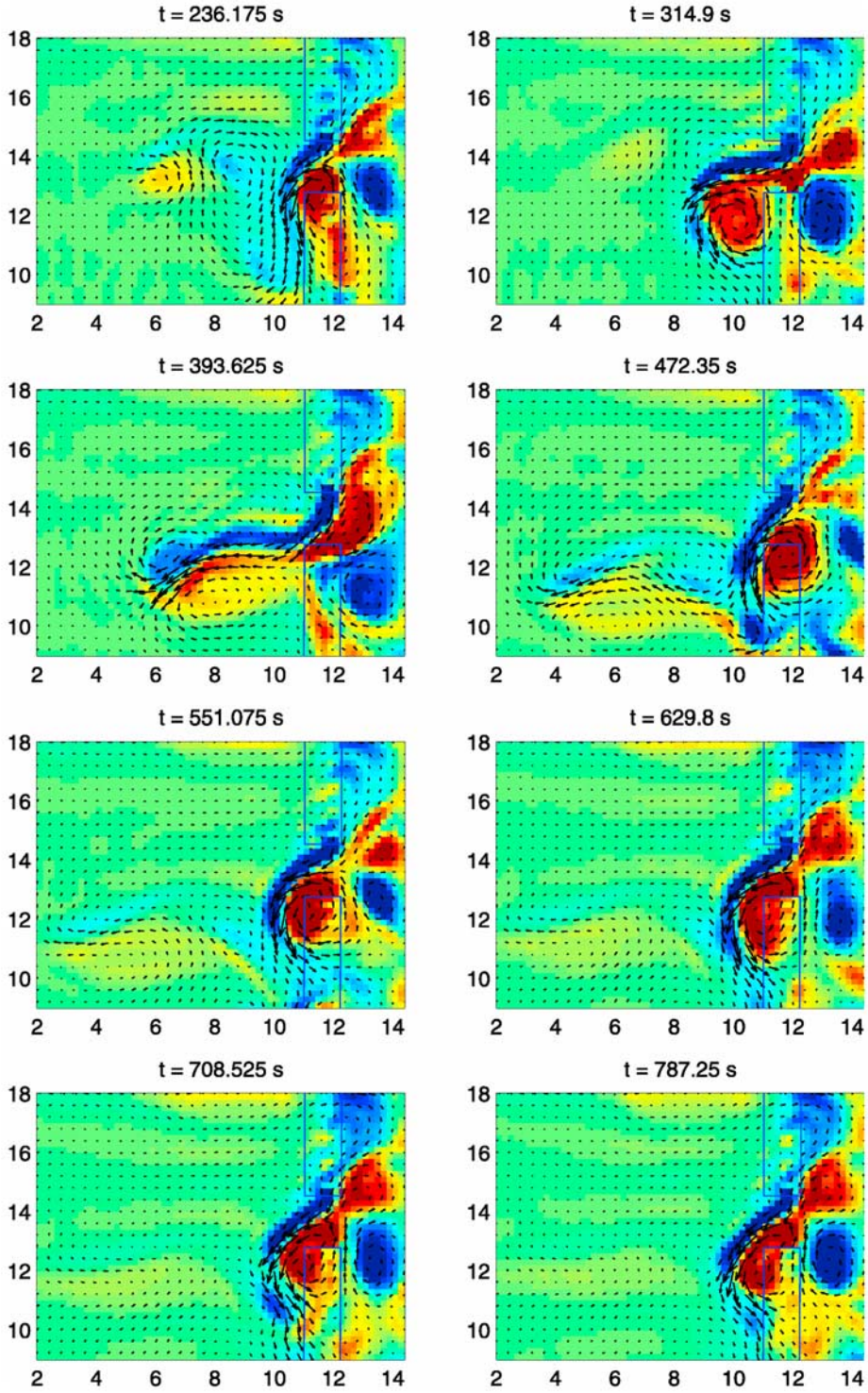

Figure 4. Instantaneous snapshots of vorticity and velocity vectors from the simulation with $f_{cw} = 0.01$. Red represents positive and blue represents negative vorticity. Only an excerpt of the entire computational domain is shown.

width of the measured rip. However, the index of agreement for the cross-shore currents is fairly good, with $d_U = 0.92$. This is again similar to the results from *Chen et al.* [1999].

[35] Figure 10 shows the longshore velocity from the experimental measurements compared with the modeled longshore currents. The modeled current velocity is a little large in Figure 10a and a little too small in Figure 10b. The offshore section (Figure 10d) shows fairly good agreement, demonstrating that the model does predict the correct bias of the rip current toward the inside of the basin. The index of

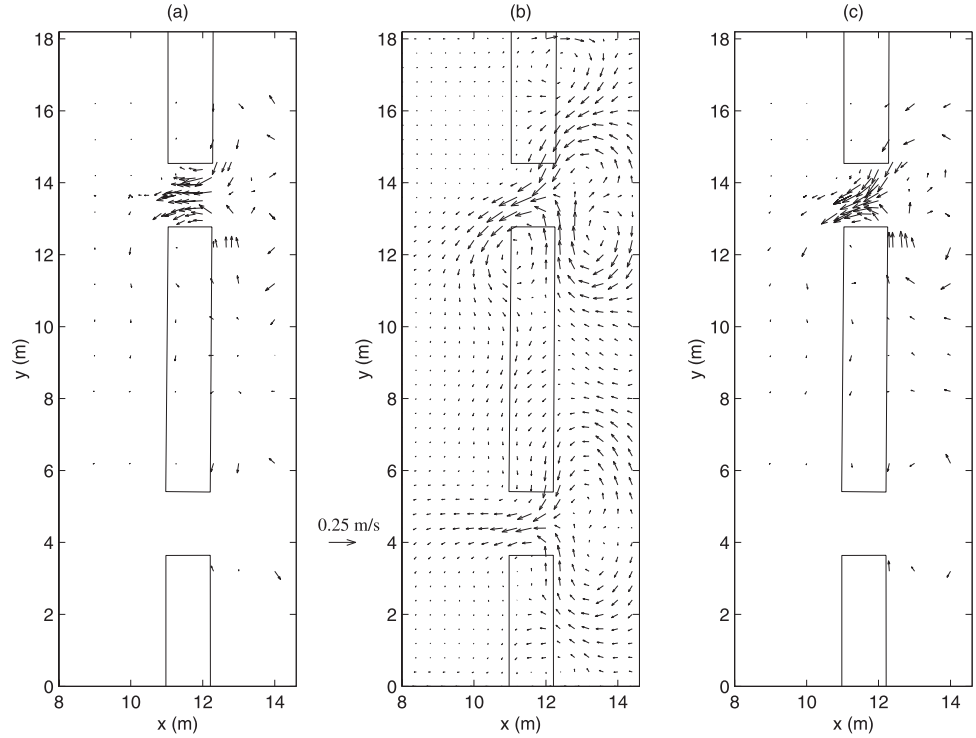

Figure 5. Time-averaged below-trough velocity ($V_{m\alpha}$) from (a) experimental data, (b) the simulation, and (c) the simulation at the same points as the experimental data.

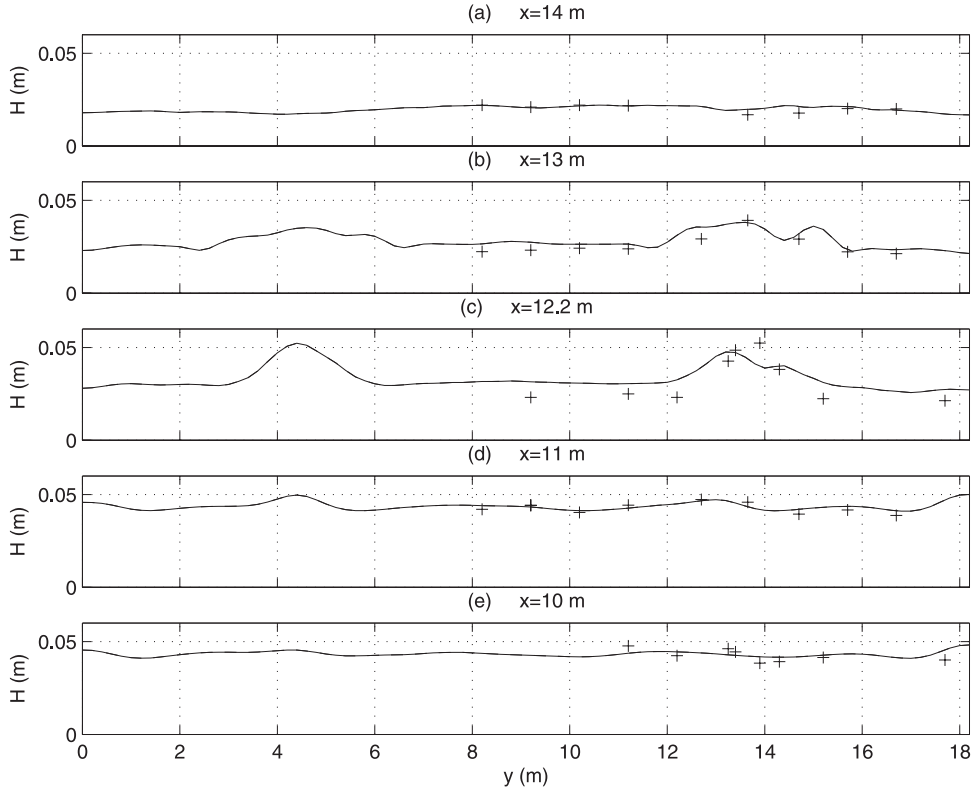

Figure 6. Comparison of time-averaged modeled wave height (line) to experimental data (pluses) for (a) x = 14 m, (b) x = 13 m, (c) x = 12.2 m, (d) x = 11 m, and (e) x = 10 m.

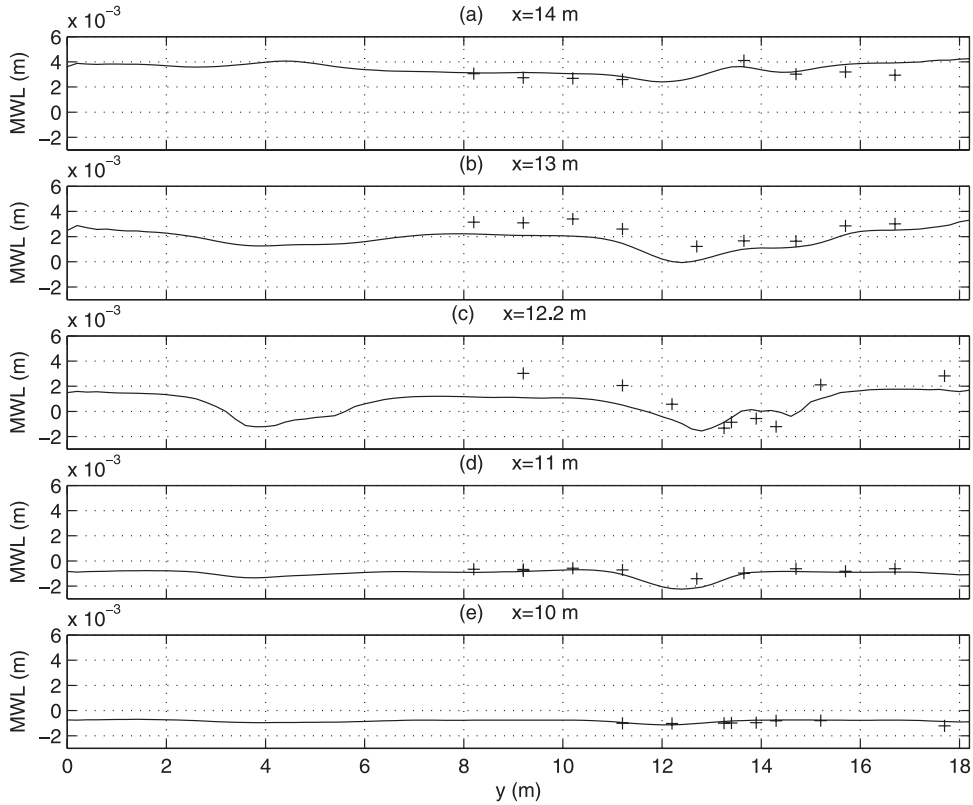

Figure 7. Comparison of time-averaged modeled mean water level (line) to experimental data (pluses) for (a) x = 14 m, (b) x = 13 m, (c) x = 12.2 m, (d) x = 11 m, and (e) x = 10 m.

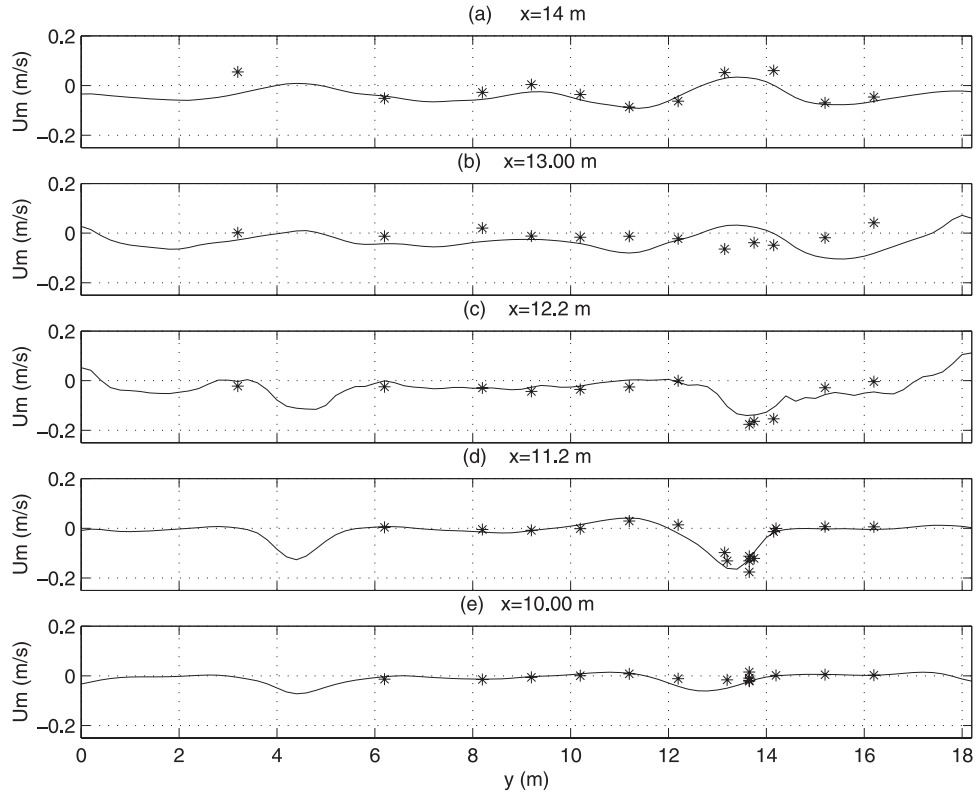

Figure 8. Comparison of time-averaged modeled cross-shore currents (line) to experimental data (asterisks) for (a) x = 14 m, (b) x = 13 m, (c) x = 12.2 m, (d) x = 11.2 m, and (e) x = 10 m.

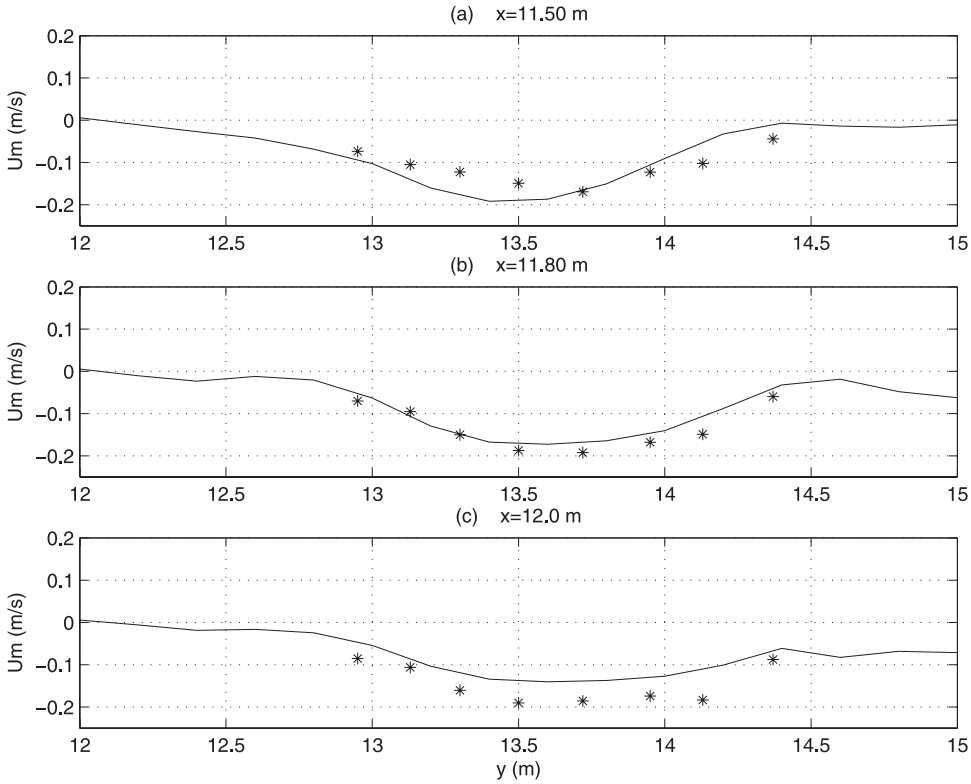

Figure 9. Comparison of time-averaged modeled cross-shore currents (line) in the channel to experimental data (asterisks) for (a) x = 11.5 m, (b) x = 11.8 m, and (c) x = 12.0 m.

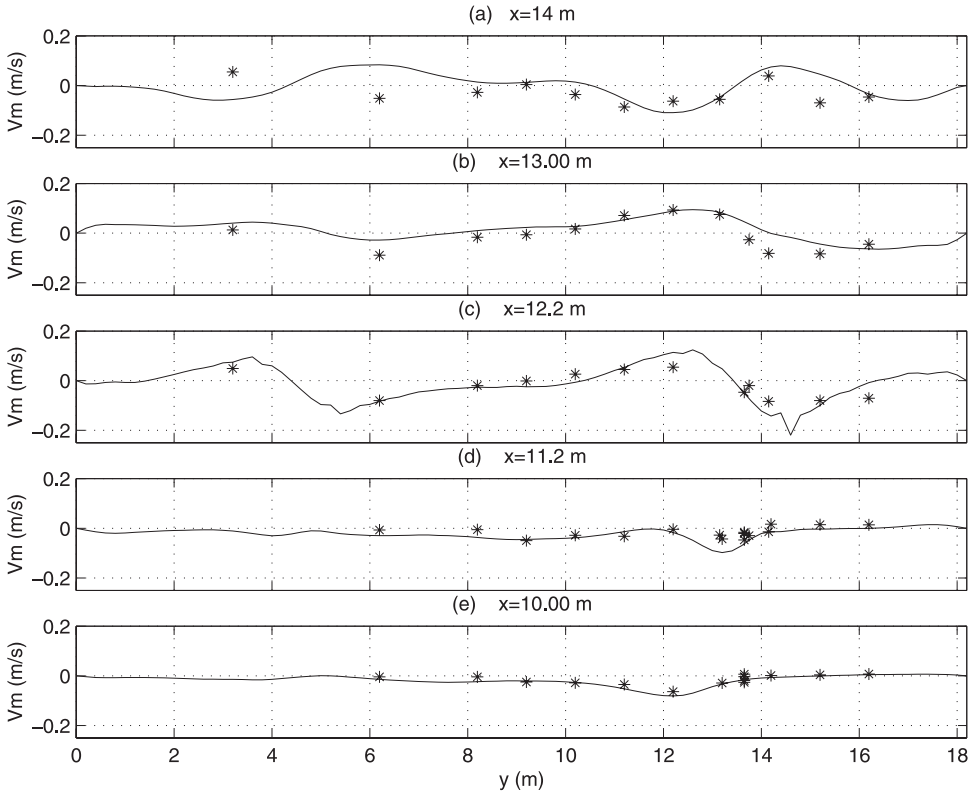

Figure 10. Comparison of time-averaged modeled longshore currents (line) to experimental data (asterisks) for (a) x = 14 m, (b) x = 13 m, (c) x = 12.2 m, (d) x = 11.2 m, and (e) x = 10 m.

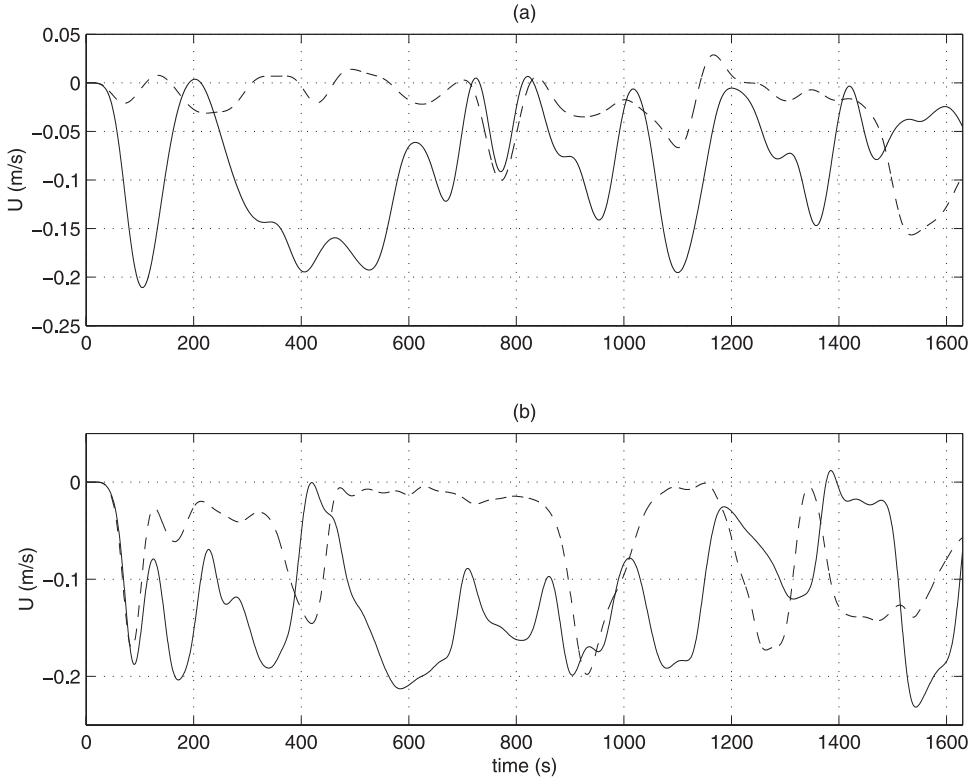

Figure 11. Low-pass filtered time series of the cross-shore velocity in the rip current at $x = 10.8$ m at $y = 13.6$ m (solid line) and $y = 4.6$ (dashed line) from (a) the measurements and (b) the SC simulation with the adjusted topography.

agreement for the longshore currents is the lowest, with $d_V = 0.80$.

[36] In summary, the results of the model simulation indicate a reasonable agreement with the measured data for the waves, mean water level and currents. On the basis of these results, in the following sections we delve into further tests and analysis of this rip current system.

4. Differences Between the Two Rips

[37] The time-averaged velocity vectors shown in Figure 5 demonstrate that the two rip channels in the wave basin produce significantly different rip behavior. The lower rip ($y = 4.6$ m) is much weaker than the upper rip ($y = 13.6$ m). Time series of the low-pass filtered cross-shore velocities measured simultaneously at the offshore edge of the channels are shown in Figure 11a. The frequency as well as the magnitude of the rip events in the lower channel ($y = 4.6$ m) are much lower than for the upper channel ($y = 13.6$ m). As shown by *Haas and Svendsen* [2000], the computed coherence for virtually all the frequencies between many sets of measurements of the two rips is well below the 90% confidence of nonzero coherence of *Thompson* [1979]. This indicates that the flows in the two rips are not related. This section establishes the behavior of the two rips in the simulations by SC and analyzes the reasons for the difference between the two rips.

[38] The design topography is completely symmetric, with the two rip channels being identical. However, the actual topography is significantly different, as an inspection of the topography in Figure 3 reveals the existence of irregularities. When the model is run for the design topography the two rips are identical. This indicates that the irregularities in the actual bathymetry are responsible for the differing rip behavior.

[39] The pattern of these variations is made clearer by subtracting the symmetric design depth h_o^{sm} from the actual still water depth h_o. A detailed look at a longshore section of the depth difference h_o-h_o^{sm} shoreward of the bar at $x = 13$ m is offered by the solid line in Figure 12. Along this section, the actual depth for $y > 7$ m is larger than the design depth, while for $y < 7$ m it is smaller than the design depth. The total depth along this section is on the order of 6 cm so that the longshore variation of ±1 cm in the depth is 15–20% of the total depth. It appears that this significant depth variation forces more feeder currents to flow toward the upper channel creating more flow in that rip. Looking back at Figure 5b confirms that more flow in the trough region behind the bar is feeding the upper rip. In fact, even in the time-averaged flow pattern, some of the flow from the recirculation cell behind the lower channel ($y = 4.6$ m) is going past the center line and feeding the upper rip ($y = 13.6$ m). Because the upper channel is fed by more of the flow over the bar, the flux in that rip is larger, leading to more instabilities. This accounts for the larger fluctuations in the time series in both the laboratory measurements and the SC simulations.

[40] In order to confirm that it is the large-scale depth variation and not the small-scale deviations causing the differences between the two rips, an adjusted topography is

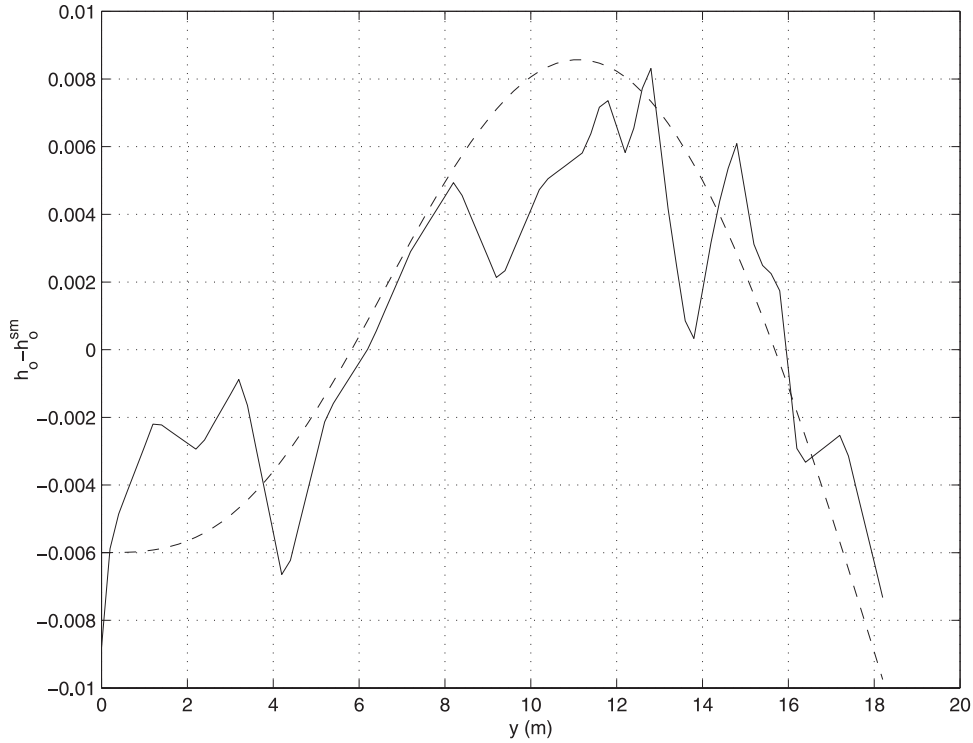

Figure 12. Longshore section in the trough shoreward of the bar at x = 13 m of the difference between h_o and h_o^{sm} for real topography (solid line) and adjusted topography (dashed line).

created by adding a smooth depression to the symmetric design topography. The difference between the adjusted and design topographies is shown by the dashed line in Figure 12. This difference is similar to the differences between the real and design topographies.

[41] Figure 11b shows time series of the cross-shore volume velocity for each rip computed by SC using the adjusted topography. It is immediately obvious from the larger velocities that the rip is much stronger in the upper channel. In addition, the fluctuations are larger and more frequent for the upper rip. Figure 13 shows the time-averaged velocity vectors for both the real bathymetry and the adjusted bathymetry. Even though the details of the flow patterns may differ, the rips in general have similar behavior for these two simulations, including the upper rip turning toward the inside of the basin.

5. Influence of the Bottom Stress

[42] One of the uncertain parameters in the simulation is the bottom shear stress. The sensitivity of the rip current system flow to this parameter is examined by running the model with a higher bottom stress coefficient than the f_{cw} = 0.01 used so far. This is accomplished by changing the bottom stress coefficient to f_{cw} = 0.025 and holding all the other parameters constant.

[43] We find that the bottom stress particularly influences the temporal variations of the current system. Specifically, increasing the friction stabilizes the flow; the rip may still meander, but only at the seaward end, and the flow in the channel is more steady. Figure 14 shows time series of the cross-shore velocity in the rip current at a point in the center of the channel for the simulations with f_{cw} = 0.01 and f_{cw} =

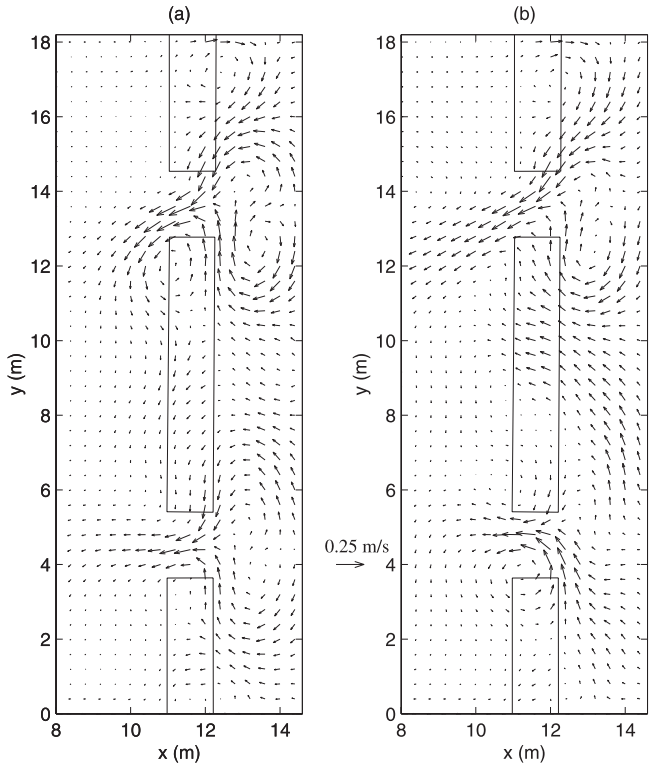

Figure 13. Time-averaged below-trough velocity ($V_{m\alpha}$) from (a) the simulation with the real bathymetry and (b) the simulation with the adjusted bathymetry.

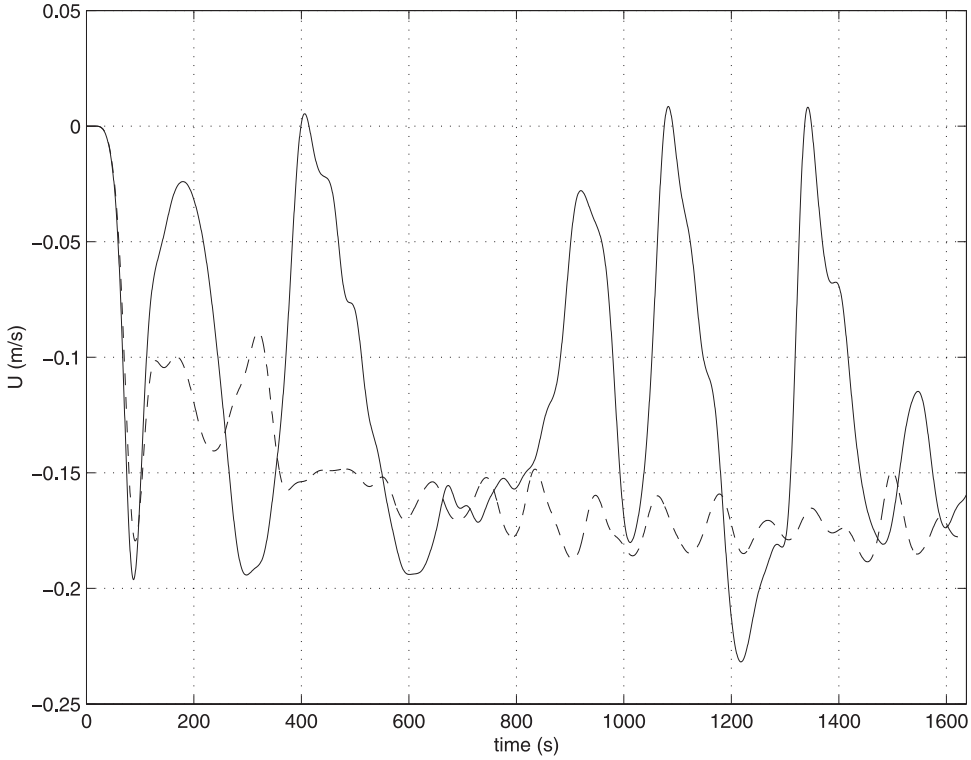

Figure 14. Low-pass filtered time series of the cross-shore velocity in the rip current at x = 11 m, y = 13.6 m from simulations with f_{cw} = 0.01 (solid line) and f_{cw} = 0.025 (dashed line).

0.025. These time series are representative of the flow at all locations in the rips. The time series with the larger friction factor shows much smaller temporal variations than the time series with the smaller friction factor. The rip current is almost constantly present, in contrast to the long intervals with the smaller f_{cw} where there is only a weak rip or no rip at all.

[44] In Figure 14 it is also clear that the instantaneous peak velocity is decreased for the larger friction factor. However, for the time-averaged currents, the alterations in the flow pattern produced by the increased friction factor are different. Figure 15 shows the time-averaged current vectors for (Figure 15a) the lower friction factor and (Figure 15b) the higher friction factor. In this figure it is apparent that for f_{cw} = 0.025 the rip current flows much farther offshore in the time-averaged sense. This is because the flow is much more stable, leading to larger time-averaged currents, whereas with the lower friction factor the current is so unstable that the rip exists at any given offshore location sporadically, so that time averaging removes the appearance of the rip.

[45] Figure 16 shows longshore sections of the cross-shore currents for model results with f_{cw} = 0.01 and f_{cw} = 0.025. The centerline of the upper rip channel is at y = 13.6 m. We see that close to the shoreline and in the trough region, Figures 16a and 16b, there is little difference between the currents for the two friction factors. In Figure 16c at the seaward edge of the bar, the current over the bar remains small, while the rip flow shifts slightly toward the outside of the basin for the higher friction factor. Again, this is a consequence of the more stable current pattern. For the section in Figure 16d which is 1 m seaward of the bar, the velocity of the rip for the higher friction factor is much

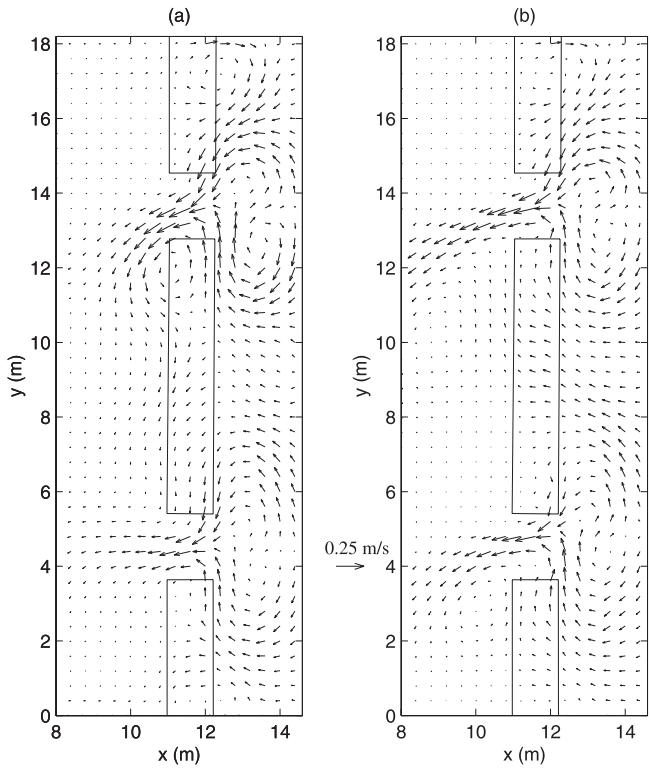

Figure 15. Time-averaged below-trough velocity ($V_{m\alpha}$) from (a) the simulation with the lower bottom stress (f_{cw} = 0.01) and (b) the simulation with higher bottom stress (f_{cw} = 0.025).

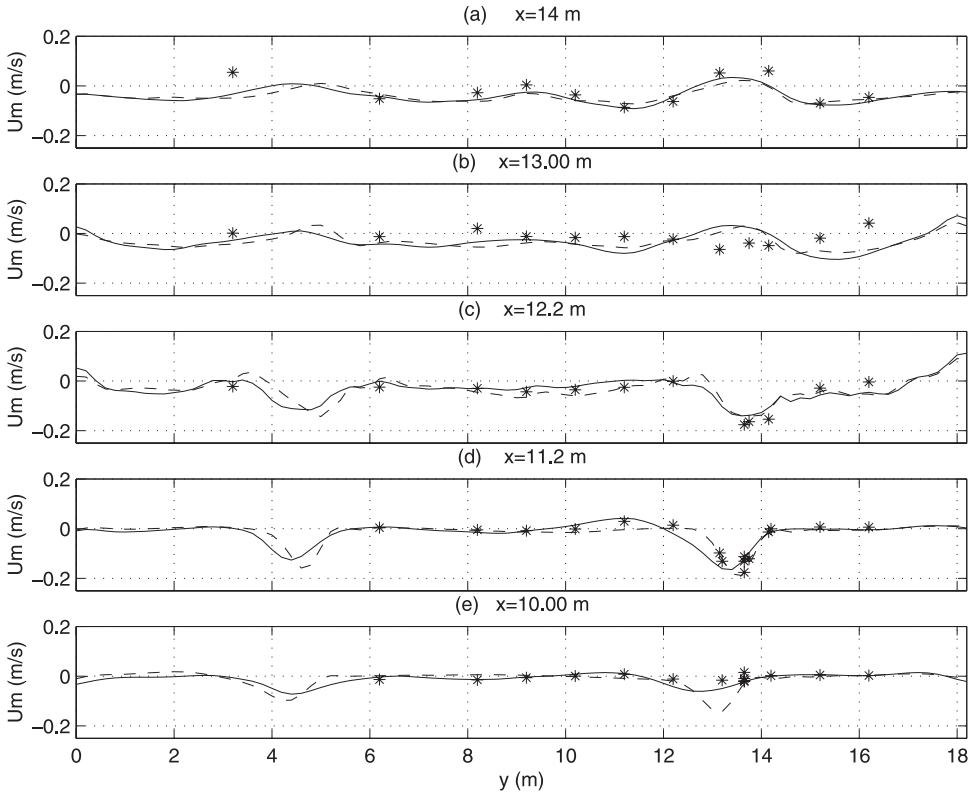

Figure 16. Comparison of time-averaged modeled cross-shore currents for $f_{cw} = 0.01$ (solid line) and $f_{cw} = 0.025$ (dashed line) to experimental data (asterisks) for (a) $x = 14$ m, (b) $x = 13$ m, (c) $x = 12.2$ m, (d) $x = 11.2$ m, and (e) $x = 10$ m.

larger than the velocity for the lower friction factor and far exceeds the measured mean velocities.

[46] Hence we find that the bottom stress contributes to the stability of rip current flows. Increasing the bottom friction leads to more stable flow patterns. Even though the increased friction results in lower instantaneous velocities, because the flow is more stable, the time-averaged rip current turns out to be larger. This may have repercussions in modeling sediment transport. For example, even though the larger friction factor produces more drag and reduces the current velocity, because the flow is also more stable, the currents persist longer at any given point. Since the sediment transport and associated bathymetric changes are a function of both the current velocity as well as the duration, the higher friction case could conceivably produce more sediment transport.

6. Significance of Wave Current Interaction

[47] When encountering opposing currents, waves increase in height and shorten in length thereby causing them to become steeper. Visual observations during the laboratory experiments of the waves in the presence of rip currents indicate that the current slows the waves in the immediate vicinity of the rip, causing the wave crest to refract such that the wave rays are focusing toward the center of the rip. It is also observed that the steepening of the waves causes them to break in the center of the rip current in or just offshore of the rip channel. This may create a radiation stress gradient which would increase the setup in the channel, reducing the longshore pressure gradient. The longshore pressure gradient is the primary driving force for the feeder currents, and the reduction in this pressure gradient would therefore decrease the feeder currents, thereby reducing the velocity of the rip current. The reduction in the rip current velocity would feed back on the waves which would become less steep, stop breaking, whence the rip would pick up again. This feedback mechanism could result in a slow pulsation of the rip current similar to observations of the experiments where the rip comes and goes, but not necessarily on a regular basis.

[48] This section discusses the effect of the wave current interaction by looking at the wave and current patterns using the model without wave current interaction and comparing this with the previous results in section 3, which include wave current interaction. In the computations without wave current interaction, the waves are calculated without any currents and are then held constant throughout the entire simulation.

[49] A comparison of the computed wave heights with and without wave current interaction with the experimental data is shown in Figure 17. This figure shows cross-shore sections of the wave height through the channel and over the center of the bar. Over the bar, the wave height with and without wave current interaction is virtually the same. However, with wave current interaction the wave height through the channel is much larger than without wave current interaction.

[50] Though these differences in wave height with and without wave current interaction may seem relatively small,

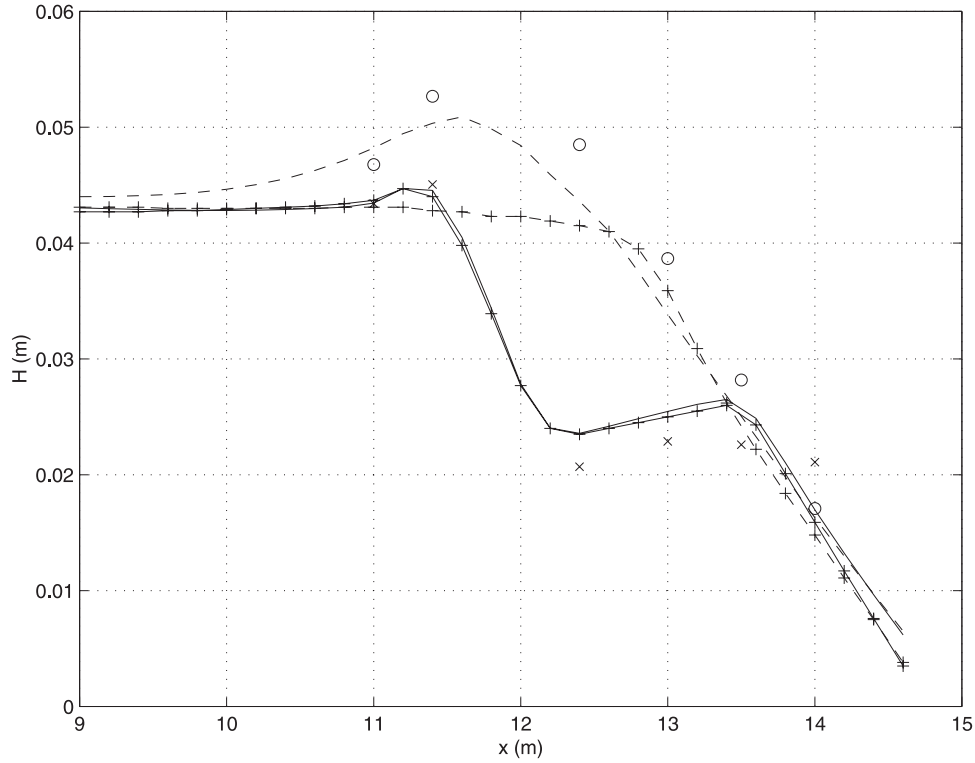

Figure 17. Comparison of time-averaged modeled wave height with wave current interaction over bar (y = 9.2 m) (solid line) and through the channel (y = 13.6 m) (dashed line), without wave current interaction over bar (y = 9.2 m) (solid line with pluses) and through channel (y = 13.6 m) (dashed line with pluses) and experimental data over bar (y = 9.2 m) (crosses) and through channel (y = 13.6 m) (circles).

the gradients are significantly different, which translates into different forcing for the currents. The resulting currents are fundamentally different from the currents with the wave current interaction. Figure 18 shows eight snapshots of vorticity and velocity vectors from the simulation without wave current interactions. Clearly, the rip extends much farther offshore than it does for the same simulations with wave current interaction in Figure 4. The rip current is still unstable, as evidenced by the meandering of the rip head and the generation of alternating eddies. This meandering resembles the instability of a jet as analyzed by *Haller and Dalrymple* [2001]. Contrarily, in Figure 4, instabilities for the simulation with wave current interaction also begin within the channel and trough in addition to the instabilities of a jet. The slow pulsation of the rip current seen visually in the experiments and in the simulation with the wave current interaction is completely absent in the simulation without wave current interaction.

[51] In order to get a better understanding of the mechanisms involved in this behavior, it is useful to realize that the two major driving mechanisms for nearshore circulation currents are the gradient of the radiation stresses $S_{\alpha\beta}$ and the pressure gradient, which is equivalent to the gradient of the mean surface elevation $\bar{\zeta}$. In some cases, like the cross-shore momentum balance on a long straight coast, these two forcing mechanisms counteract and nearly balance each other with only a small difference of about 5% of the radiation stress gradient actually available to drive the circulation currents such as the undertow for this case. On the other hand, in the longshore momentum balance on a longshore uniform situation, there is no pressure gradient, and the entire longshore component of the radiation stress is available for driving the longshore current.

[52] In a more complicated situation like rip currents, it is the vectorial sum of the two forcing terms that indicates how much net forcing is available to drive currents. The forcing residual R_α is defined as

$$R_\alpha = -\frac{1}{\rho}\frac{\partial S_{\alpha\beta}}{\partial x_\beta} - gh\frac{\partial \bar{\zeta}}{\partial x_\alpha}. \tag{18}$$

[53] We use the forcing residual concept to examine the mechanism behind the slow pulsation of the rip current. First, Figure 19 shows longshore sections at x = 11 m (which is at the offshore edge of the channel) of the cross-shore velocity in the rip at different times. Initially, there is a strong rip (illustrated at t = 519 s) with velocities exceeding 20 cm/s. In subsequent snapshots the rip velocity is decreasing, under 10 cm/s by t = 645 s, and the rip has virtually vanished by t = 897 s. However, the rip does come back by t = 960 s.

[54] Assuming that the currents observed in Figure 19 at x = 11 m can be related to the cross-shore forcing located 1 m shoreward at x = 12 m, we show in Figure 20 the x-component of the forcing residual R_x for the corresponding times. We see that at t = 519 s the forcing residual in the center of the rip channel is large. However, with time, R_x decreases significantly in the channel, thereby decreasing the

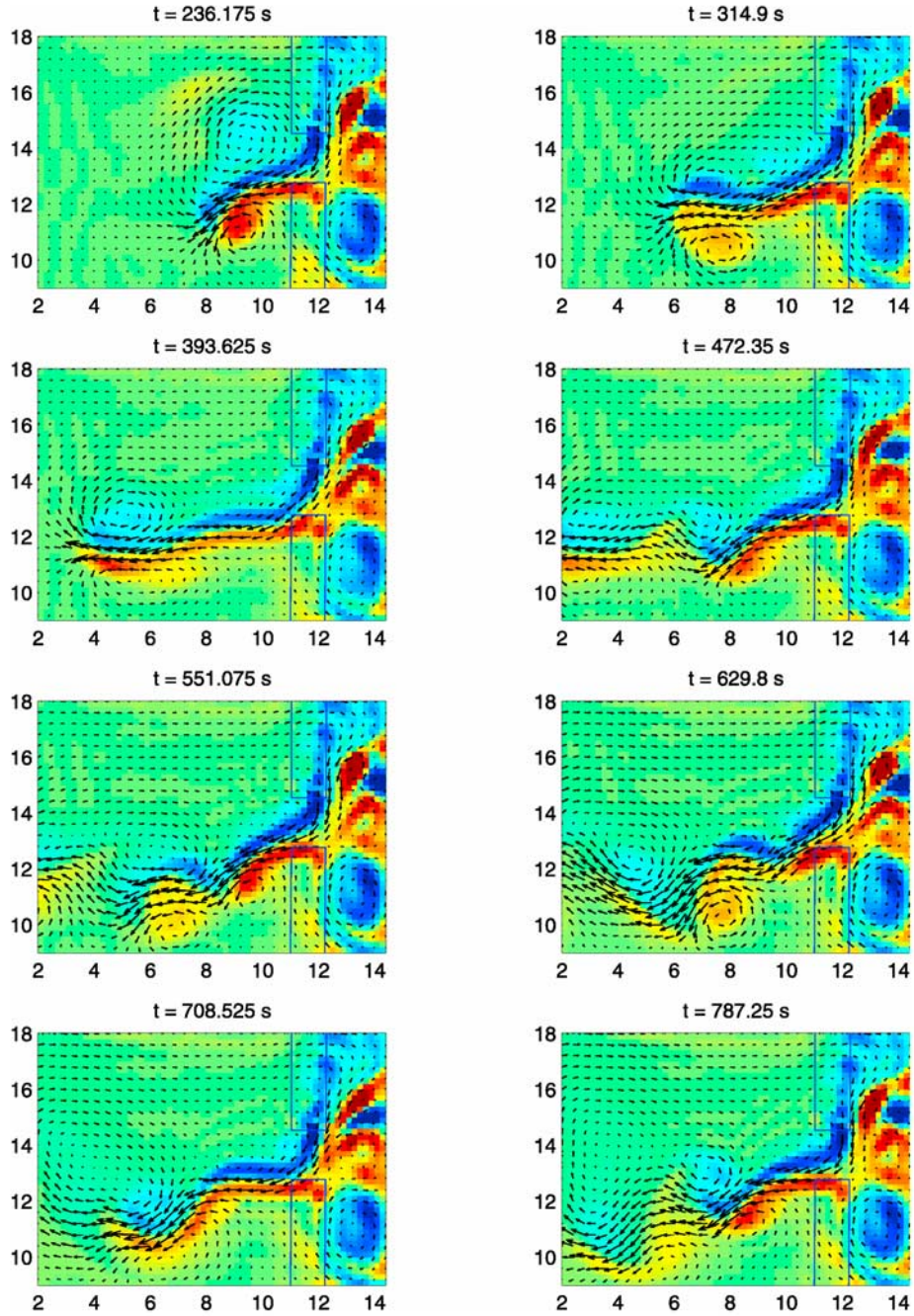

Figure 18. Instantaneous snapshots of vorticity and velocity vectors from SC without wave current interaction showing the rip current extending far offshore. Red represents positive and blue represents negative vorticity. Only an excerpt of the entire computational domain is shown.

rip velocity. In the first two snapshots at t = 519 and 582 s, the pressure gradient is virtually identical. At t = 519 s, Figure 19 shows a strong rip current. However, examination of the model results show that at this time the waves are not yet breaking in the channel so the radiation stress gradients are still small. By t = 582 s the strong rip current has forced the waves to break in the channel, creating a radiation stress gradient in the channel. This radiation stress gradient opposes the pressure gradient and decreases the residual forcing and decreases the rip velocity. As the rip velocity decreases, the waves in the channel stop breaking, and eventually, by t = 960 s, the residual forcing is large again, as there is no radiation stress gradient; therefore, at that time the rip velocity is again large.

[55] This is not meant to imply that these slow rip pulsations are only related to the local cross-shore forcing. This forcing itself is connected to the flow patterns in the entire rip current system. For example, the large cross-shore pressure gradient driving the rip flow offshore is the result of the converging feeder currents. As these feeder currents

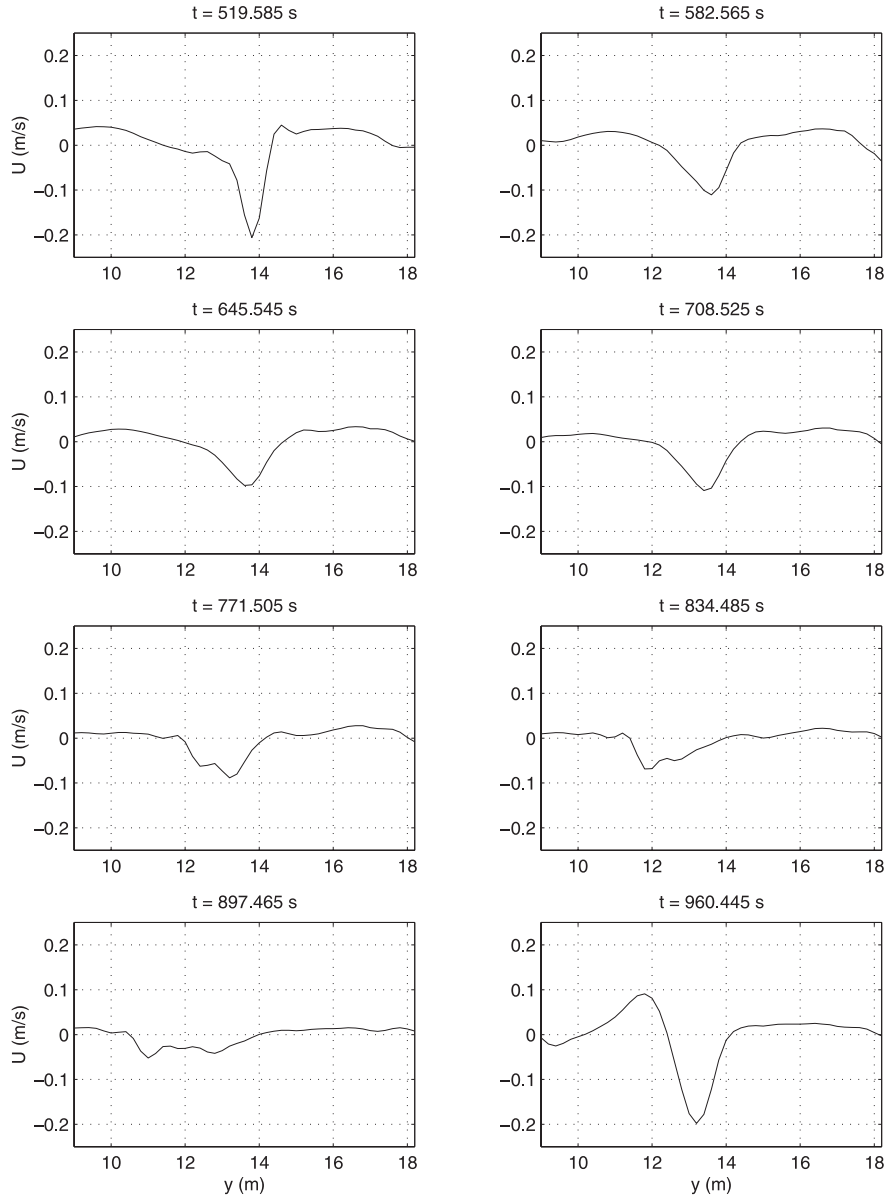

Figure 19. Snapshots in time of longshore sections of the cross-shore velocity at the offshore edge of the channel (x = 11 m) showing the slow pulsation of the rip current. The channel is centered at y = 13.6 m.

weaken due to decreases in the longshore pressure gradient when waves break in the channel, the cross-shore pressure gradient and therefore the residual forcing is smaller, driving weaker rip currents.

[56] Because this pulsation mechanism involves the entire rip system, it is a slow process lasting hundreds of seconds, and in the experiments it has primarily been observed visually. These fluctuations are also much slower than the higher-frequency oscillations which may be linked to the instability of turbulent jet flow [*Haller and Dalrymple*, 2001]. An important question is why do the waves and currents never reach an equilibrium? In simulations with other conditions where the rip is stronger (such as test C from *Haller et al.* [2002]), the waves and currents appear to achieve an equilibrium balance such that this pulsation mechanism is no longer present. A more extensive study is required to determine under which conditions the waves and currents are balanced and under which conditions the pulsation mechanism is present; however, the evidence suggests that it is linked to the wave current interaction.

7. Significance of 3D Currents

[57] The advantage of using quasi-3D models over other types of nearshore circulation models is that they include the effect of the vertical variation in direction and magnitude of the current velocities. The wave-current and current-current interactions result in terms with dispersive lateral mixing properties. *Svendsen and Putrevu* [1994] previously found for the case of a longshore uniform longshore current, that these terms provide 95% or more of the lateral mixing even inside the surfzone. Unlike empirical mixing formulations, the 3D mixing mechanism cannot be tuned to match data. It does depend on the eddy viscosity, but only to get

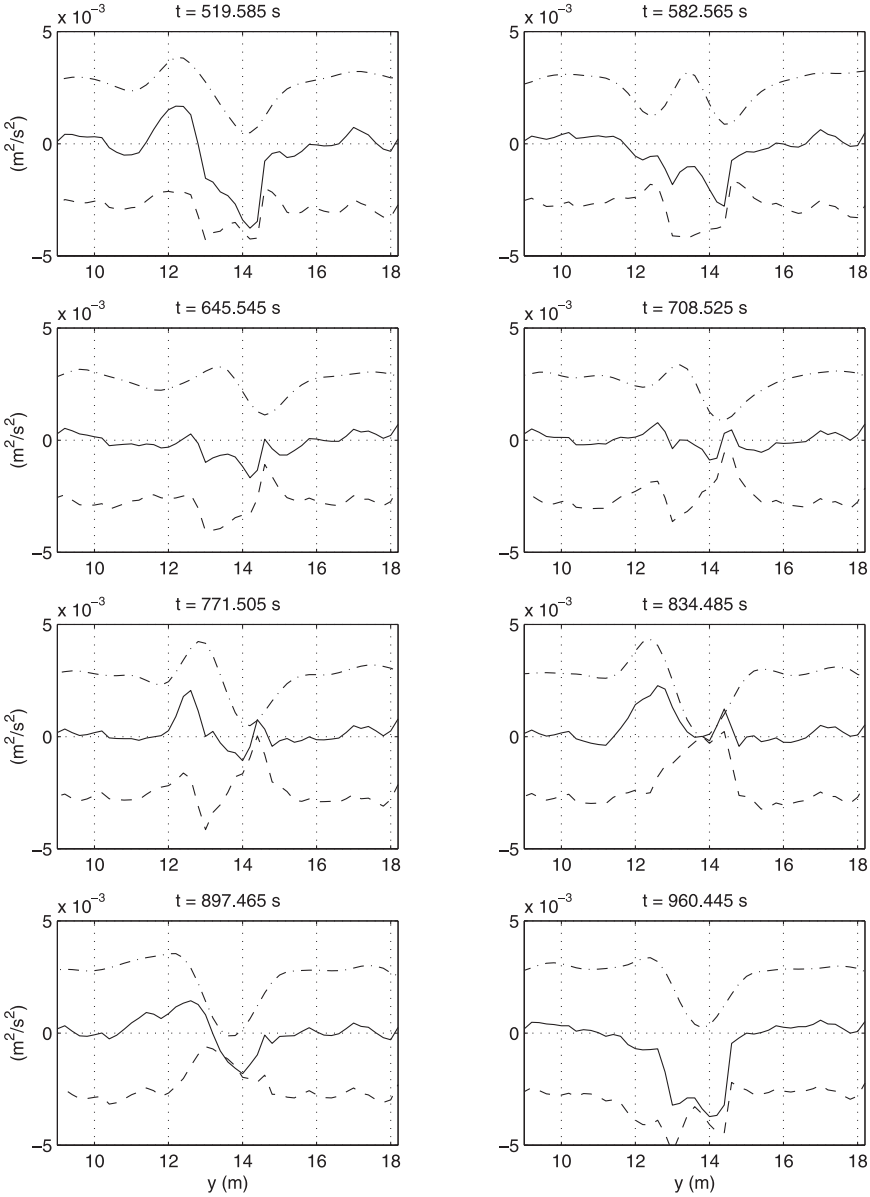

Figure 20. Snapshots in time of longshore sections of the cross-shore forcing residual R_x (solid line), pressure gradient $-gh\frac{\partial \bar{\zeta}}{\partial x}$ (dashed line), and the radiation stress gradient $-\frac{1}{\rho}\frac{\partial S_{x\beta}}{\partial x_\beta}$ (dash-dotted line) at x = 12 m. This is the forcing 1 m shoreward of the rip current sections shown in Figure 19. The channel is centered at y = 13.6 m.

the vertical profile of the current correct as shown for rip currents by *Haas and Svendsen* [2000] and *Haas et al.* [2000]. The significance of the three dimensionality of the rip current system is analyzed in this section by comparing with the results of 2D simulations, which corresponds to considering depth uniform currents.

[58] When doing computations for depth uniform currents, all the dispersive mixing terms are exactly zero. The only mixing in the model then comes from the turbulent mixing due to the wave breaking, the bottom friction, and the horizontal shear in the flow. This turbulent mixing is typical of the lateral mixing which is commonly included in circulation models. Figure 21 shows eight snapshots of the vorticity and current vectors from the simulation for depth uniform currents. We see that the currents are much more unstable in this figure than for the simulation with depth varying currents and 3D mixing in Figure 4. The eddies, which are created and shed by the rip, drift around the domain and take a long time to dissipate. In the three-dimensional simulation the rip also generates eddies; however, as Figure 4 shows, these eddies do not float freely around and are dissipated much more rapidly.

[59] Another important illustration of the 3D effects on the flow pattern is shown in Figure 22, with the time-averaged velocity vectors for simulation with 3D currents in Figure 22a and from the simulation for depth uniform currents in Figure 22b. Because of the highly unstable nature of the flow without the 3D dispersive mixing mechanism, the time-averaged rip is much broader in Figure 22b than in Figure 22a. Also, since the rip meanders

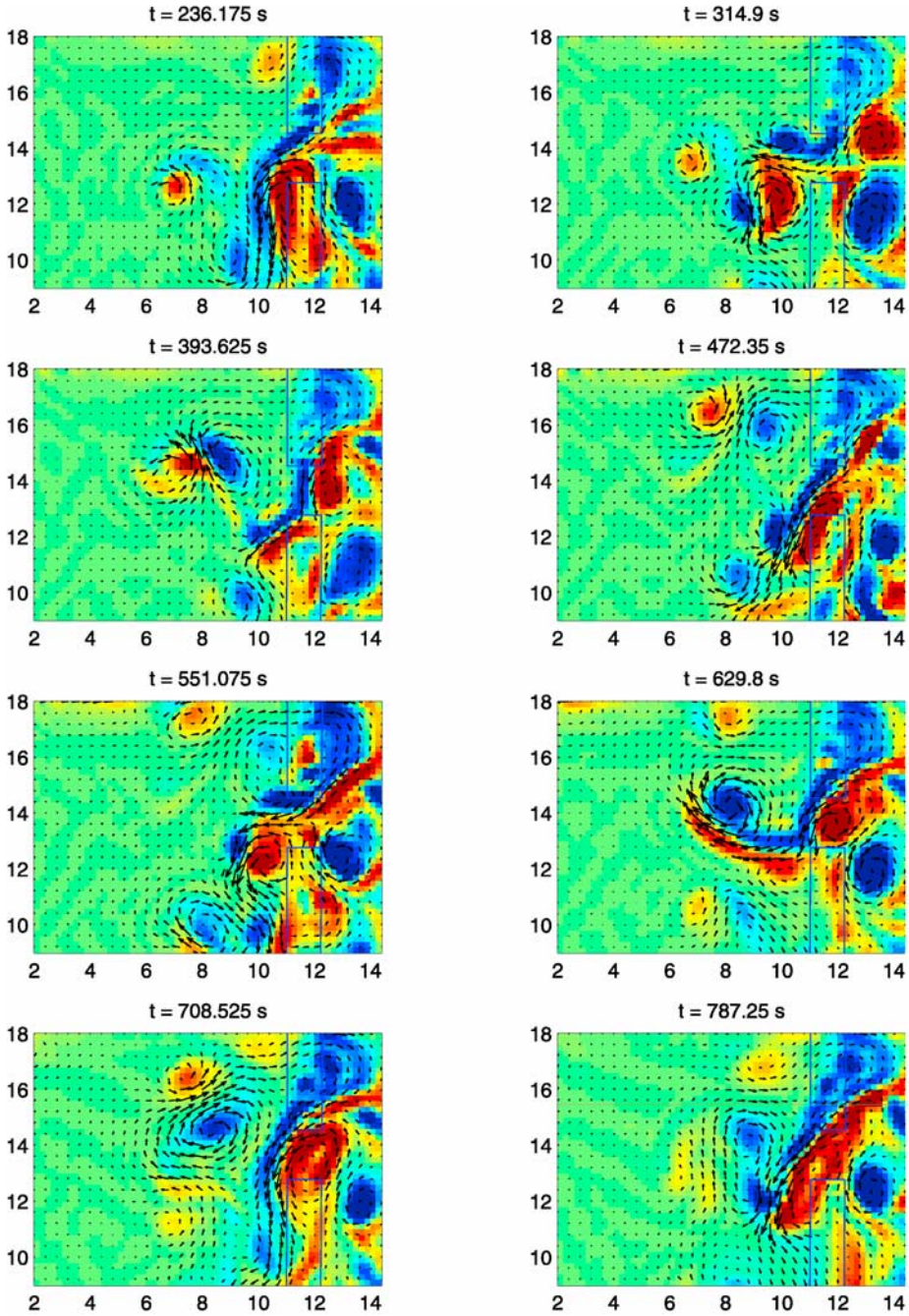

Figure 21. Instantaneous snapshots of vorticity and velocity vectors from the simulation without 3D dispersive mixing (i.e., depth uniform currents). Red represents positive and blue represents negative vorticity. Only an excerpt of the entire computational domain is shown. Comparison with Figure 4 show that the flow is much more unstable with depth uniform currents.

to both sides, the time average does not appear to be biased to any particular side. Inspecting the flow over the center of the bar between the rips reveals that in the case of depth uniform flow there is a significant return current over this bar. Eddies which are generated in the trough region behind the bar, but not dissipated, actually pass over the center of the bar, resulting in a net flow seaward, a feature which does not appear as strongly when the 3D effects are included.

[60] Figures 23 and 24 show the relative magnitudes of the 3D and turbulent mixing in the momentum balances offshore of the bar and shoreward of the bar, respectively. Offshore of the bar in Figure 23, the mixing occurs primarily in the region of the rip indicated by the location of large offshore directed velocities in Figure 23a. The 3D mixing (solid lines) is much larger than the turbulent mixing (dashed lines) because the waves are not breaking, leaving only bottom stress and subgrid stress contributions to the

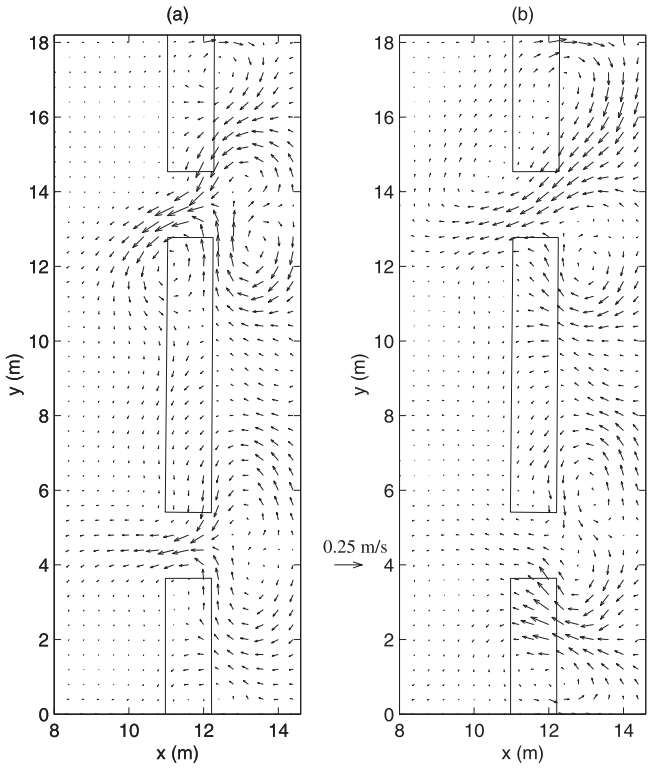

Figure 22. Time-averaged below-trough velocity ($V_{m\alpha}$) from (a) the 3D simulation and (b) the 2D simulation.

turbulence. In addition, the distribution of the mixing is much different, which prevents the turbulent mixing from replacing the 3D mixing simply by increasing the magnitude of the coefficients. In Figure 24 behind the bar in the feeder currents, indicated by the large longshore currents in Figure 24a, the turbulent mixing is still much smaller than the 3D mixing. Again, the distribution of the mixing is quite different.

[61] Hence the flow patterns for the simulations using depth uniform currents are significantly different from the flow patterns for the simulations with the depth varying currents and observations from the experiment. Eddies generated by the rip currents in the 2D simulation are dispersed much slower and tend to fill the entire computational domain. Increasing the bottom friction similarly decreases the fluctuations in the flow patterns. However, as shown in section 5, the resulting flow pattern when increasing the bottom stress is much less reasonable than the measurements indicate. This suggests that including the three dimensionality of the currents results in a strong mixing mechanism for rip current systems, making it useful to include this mechanism when simulating rip currents.

8. Conclusions

[62] The numerical nearshore circulation model SHORECIRC has been used to simulate the currents generated in a closed directional wave basin and compared with the experiments by *Haller et al.* [2002]. The time-averaged

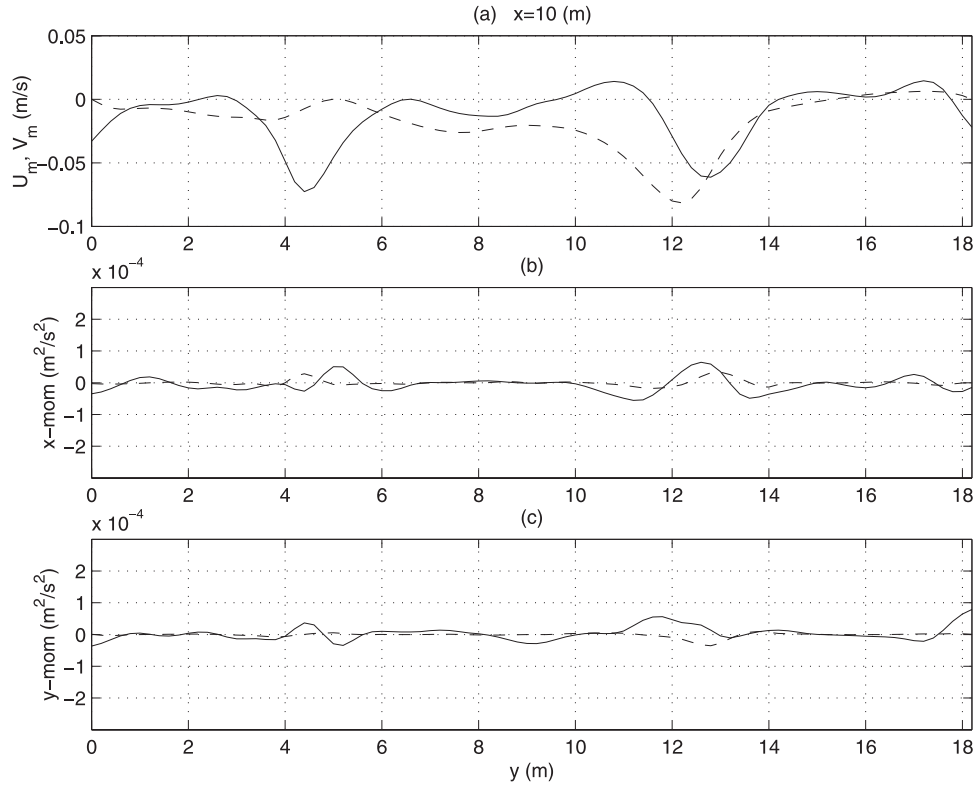

Figure 23. Longshore sections offshore of the bar at x = 10 m of time-averaged (a) cross-shore (solid line) and longshore velocity (dashed line), (b) cross-shore 3D mixing terms (solid line) and turbulent mixing terms (dashed line), and (c) longshore 3D mixing terms (solid line) and turbulent mixing terms (dashed line). The channels are centered at y = 4.6 and 13.6 m.

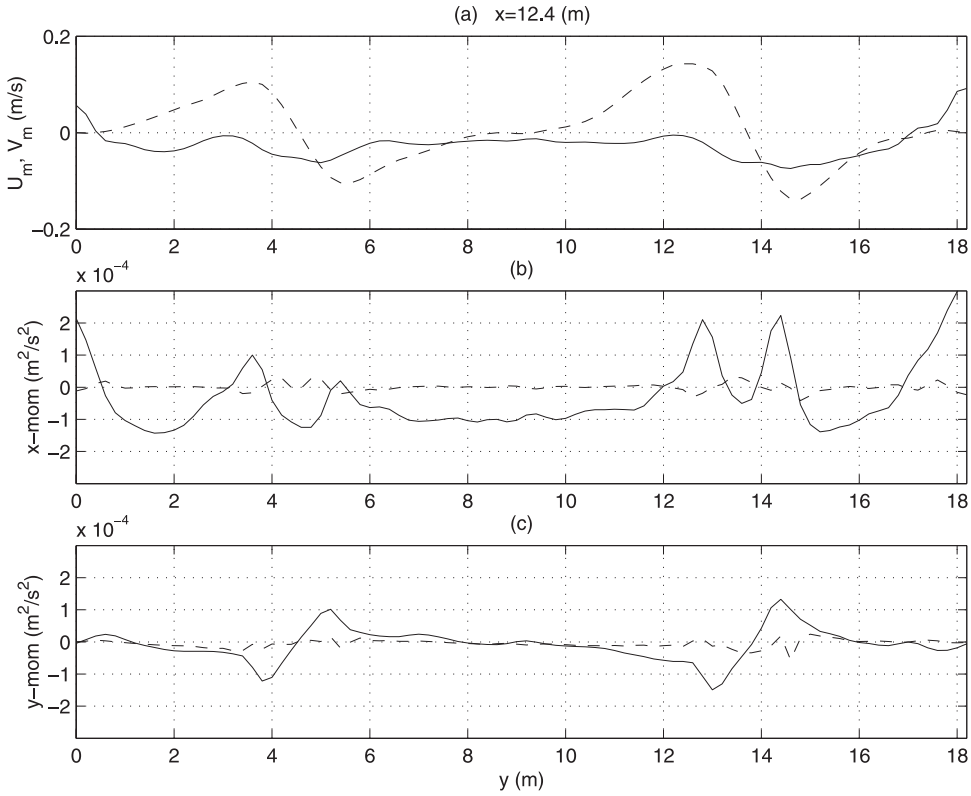

Figure 24. Longshore sections shoreward of the bar at x = 12.4 m of time-averaged (a) cross-shore (solid line) and longshore velocity (dashed line), (b) cross-shore 3D mixing terms (solid line) and turbulent mixing terms (dashed line), and (c) longshore 3D mixing terms (solid line) and turbulent mixing terms (dashed line). The channels are centered at y = 4.6 and 13.6 m.

flow properties from the model are compared with the time-averaged measurements, and the overall results show reasonable agreement between the model and laboratory data. The *Wilmott* [1981] index of agreement between the model and data is found to be quite good. Thus computations with the model provide much deeper insight into the flow mechanisms than can be gained from the measurements alone.

[63] First, it is noted that the rips in the two channels behaved differently. The rip in the upper channel where most of the analysis takes place is much stronger than the lower rip. The cause of this difference is the depth difference across the basin. The depth is greater on the upper half (y > 7 m) of the basin causing more flow toward the upper rip channel leading to a stronger rip current.

[64] Second, the bottom stress affects the stability of the rip current. Higher bottom stress leads to more stable flow where the rip current meanders less and fewer eddies are generated. Even though the higher friction reduces the magnitude of the instantaneous velocity in the rip current, the time-averaged velocity of the rip current increases because the flow fluctuates less. Because of the significant impact it has on the flow, this could help estimate realistic values of the bottom friction factor.

[65] Third, wave current interaction appears to be important in rip current systems. Observations during the laboratory experiments indicated that the wave heights increase in the presence of the rip and that the waves and the rip may interact, creating a slow pulsation of the rip. The modeled wave heights show increases in wave height in the channels in the presence of the rip current. The wave current interaction in the model creates forcing which appears to reduce the distance the rip currents flow offshore and seems to produce the slow pulsation which may have been observed in the experiments. Several basic features observed in both experimental and numerical simulation results indicate that rip currents have additional features beyond simple unstable jets. Wave current interaction may play an important and previously unexamined role in the unsteady behavior of rip currents. However, additional modeling and more extensive simultaneous measurements are required to validate this pulsation mechanism.

[66] Finally, the significance of the three dimensionality of the currents is demonstrated. The flow patterns are much more stable when this mechanism is included. Increased bottom stress also makes the flow more stable; however, the resulting flow patterns in that case are much different from the observed flow patterns. The model runs with depth uniform currents are less stable and the generated eddies disperse slower and tend to fill the computational domain with isolated, freely drifting vortices, and the time-averaged rip pattern shows less similarity with the measured pattern.

[67] The preceding conclusions specifically pertain to the laboratory scale rip current system that is being modeled. However, additional work including measurements and modeling of different wave conditions would be useful in extending and validating these conclusions. Also, it will be beneficial to test these results based on rip current systems

in the field. In addition, it would improve the work to utilize a more accurate wave theory to better represent the short-wave forcing for rip current systems.

[68] **Acknowledgments.** This work was sponsored by Sea Grant, under award NA96RG0029, and the National Oceanographic Partnership Program by ONR (contract N0014-99-1-1051).

References

Aagaard, T., B. Greenwood, and J. Nielsen, Mean currents and sediment transport in a rip channel, *J. Mar. Geol.*, *140*, 25–45, 1997.

Arthur, R. S., A note on the dynamics of rip currents, *J. Geophys. Res.*, *67*, 2777–2779, 1962.

Battjes, J. A., Modelling of turbulence in the surfzone, paper presented at Symposium on Modelling Techniques, Am. Soc. Civ. Eng., Reston, Va., 1975.

Bowen, A. J., Rip currents: 1. Theoretical investigations, *J. Geophys. Res.*, *74*, 5467–5478, 1969.

Bowen, A. J., and D. L. Inman, Rip currents: 2. Laboratory and field observations, *J. Geophys. Res.*, *74*, 5479–5490, 1969.

Brander, R. W., Field observations on the morphodynamic evolution of a low-energy rip current system, *J. Mar. Geol.*, *157*, 199–217, 1999.

Chen, Q., R. A. Dalrymple, J. T. Kirby, A. B. Kennedy, and M. C. Haller, Boussinesq modeling of a rip current system, *J. Geophys. Res.*, *104*, 20,617–20,637, 1999.

Coffey, F. C., and P. Nielsen, Aspects of wave current boundary layer flows, paper presented at 19th Coastal Engineering Conference, Am. Soc. Civ. Eng., Houston, Tex., 1984.

Dalrymple, R. A., Rip currents and their causes, paper presented at 14th Coastal Engineering Conference, Am. Soc. Civ. Eng., Reston, Va., 1978.

Dalrymple, R. A., and C. J. Lozano, Wave-current interaction models for rip currents, *J. Geophys. Res.*, *83*, 6063–6071, 1978.

Dette, H.-H., K. Peters, and F. Spignat, About rip currents at a mesotidal coast, paper presented at Coastal Dynamics '95, Am. Soc. Civ. Eng., Gdansk, Poland, 1995.

Drønen, N., H. Karunarathna, J. Fredsøe, B. M. Sumer, and R. Deigaard, An experimental study of rip channel flow, *Coastal Eng.*, *45*, 223–238, 2002.

Haas, K. A., and I. A. Svendsen, Three-dimensional modeling of rip current systems, *Res. Rep. CACR-00-06*, Cent. for Appl. Coastal Res., Univ. of Del., Newark, Del., 2000.

Haas, K. A., and I. A. Svendsen, Laboratory measurements of the vertical structure of rip currents, *J. Geophys. Res.*, *107*, 3047, doi:10.1029/2001JC000911, 2002.

Haas, K. A., I. A. Svendsen, and Q. Zhao, 3D modeling of rip currents, paper presented at 27th Coastal Engineering Conference, Am. Soc. Civ. Eng., Sydney, 2000.

Haller, M. C., and R. A. Dalrymple, Rip current instabilities, *J. Fluid Mech.*, *433*, 161–192, 2001.

Haller, M. C., R. A. Dalrymple, and I. A. Svendsen, Experimental study of nearshore dynamics on a barred beach with rip channels, 2002, *J. Geophys. Res.*, *107*, 3061, doi:10.1029/2001JC000955, 2002.

Hamm, L., Directional nearshore wave propagation over a rip channel: An experiment, paper presented at 23rd Coastal Engineering Conference, Am. Soc. Civ. Eng., Venice, Italy, 1992.

Hoffman, J. D., *Numerical Methods for Engineers and Scientist*, McGraw-Hill, New York, 1992.

Kirby, J. T., and R. A. Dalrymple, A parabolic equation for the combined refraction-diffraction of stokes waves by mildly varying topography, *J. Fluid Mech.*, *136*, 453–466, 1983.

Kirby, J., and R. Dalrymple, Combined refraction/diffraction model REF/DIF 1, version 2.5, *Tech. Rep. CACR-94-22*, Cent. for Appl. Coastal Res., Univ. of Del., Newark, Del., 1994.

Lippmann, T. C., and R. A. Holman, The spatial and temporal variability of sand bar morphology, *J. Geophys. Res.*, *95*, 11,575–11,590, 1990.

McKenzie, P., Rip current systems, *J. Geol.*, *66*, 103–113, 1958.

Mei, C., *The Applied Dynamics of Ocean Surface Waves*, John Wiley, New York, 1983.

Nadaoka, K., and T. Kondoh, Laboratory measurements of velocity field structure in the surfzone by LDV, *Coastal Eng. Jpn.*, *25*, 125–145, 1982.

Noda, E. K., Wave-induced nearshore circulation, *J. Geophys. Res.*, *79*, 4097–4106, 1974.

Phillips, O. M., *The Dynamics of the Upper Ocean*, Cambridge Univ. Press, New York, 1977.

Putrevu, U., and I. A. Svendsen, Wave induced nearshore currents: a study of the forcing, mixing and stability characteristics, *Res. Rep. CACR-91-11*, Cent. for Appl. Coastal Res., Univ. of Del., Newark, Del., 1991.

Putrevu, U., and I. A. Svendsen, Three-dimensional dispersion of momentum in wave-induced nearshore currents, *Eur. J. Mech. B/Fluids*, *18*(3), 409–427, 1999.

Sancho, F., and I. A. Svendsen, Unsteady nearshore currents on longshore varying topographies, *Res. Rep. CACR-97-10*, Cent. for Appl. Coastal Res., Univ. of Del., Newark, Del., 1997.

Shapiro, R., Smoothing, filtering and boundary effects, *Rev. Geophys.*, *8*, 359–387, 1970.

Shepard, F. P., Undertow, rip tide or rip current, *Science*, *84*, 181–182, 1936.

Shepard, F. P., and D. L. Inman, Nearshore water circulation related to bottom topography and wave refraction, *Eos Trans. AGU*, *31*, 196–212, 1950.

Shepard, F. P., K. O. Emery, and E. La Fond, Rip currents: A process of geological importance, *J. Geol.*, *49*, 337–369, 1941.

Short, A. D., Three dimensional beach-stage model, *J. Geol.*, *87*, 553–571, 1979.

Smagorinsky, J., General circulation experiments with the primitive equations: I. The basic experiment, *Mon. Weather Rev.*, *91*, 99, 1963.

Smith, J. A., and J. L. Largier, Observations of nearshore circulation: Rip currents, *J. Geophys. Res.*, *100*, 10,967–10,975, 1995.

Sonu, C. J., Field observations of nearshore circulation and meandering currents, *J. Geophys. Res.*, *77*, 3232–3247, 1972.

Svendsen, I. A., Wave heights and set-up in a surf zone, *Coastal Eng.*, *8*, 303–329, 1984a.

Svendsen, I. A., Mass flux and undertow in a surf zone, *Coastal Eng.*, *8*, 347–365, 1984b.

Svendsen, I. A., Analysis of surf zone turbulence, *J. Geophys. Res.*, *92*, 5115–5124, 1987.

Svendsen, I. A., and U. Putrevu, Nearshore circulation with 3-d profiles, paper presented at 22nd Coastal Engineering Conference, Am. Soc. Civ. Eng., Delft, Netherlands, 1990.

Svendsen, I. A., and U. Putrevu, Nearshore mixing and dispersion, *Proc. R. Soc. London, Ser. A*, *445*, 1–16, 1994.

Tanaka, H., and A. Wada, Reproduction of nearshore currents by a mathematical model, *Coastal Eng. Jpn.*, *27*, 151–163, 1984.

Thompson, R., Coherence significance levels, *J. Atmos. Sci.*, *36*, 2020–2021, 1979.

Wilmott, C. J., On the validation of models, *Phys. Geogr.*, *2*, 184–194, 1981.

Wright, L., and A. D. Short, Morphydynamic variability of surf zones and beaches: A synthesis, *Mar. Geol.*, *56*, 93–118, 1984.

You, Z.-J., A simple model for current velocity profiles in combined wave-current flows, *Coastal Eng.*, *23*, 289–304, 1994.

K. A. Haas, Georgia Tech Regional Engineering Program, 6001 Chatham Center Drive, Savannah, GA 31405, USA. (kevin.haas@gtrep.gatech.edu)

M. Haller, 202 Apperson Hall, Civil, Construction and Environmental Engineering, Oregon State University, Corvallis, OR 97331-2302, USA. (hallerm@engr.orst.edu)

I. A. Svendsen and Q. Zhao, Center for Applied Coastal Research, Ocean Engineering Laboratory, University of Delaware, Newark, DE 19716, USA. (ias@coastal.udel.edu; zhao@coastal.udel.edu)